Assessing Compressive Properties of GFRP Bars: Novel Test Fixture and Statistical Analysis

Alireza Sadat Hosseini[1*] and Pedram Sadeghian[2]

[1] Research Assistant, Department of Civil and Resource Engineering, Dalhousie University, Canada

[2] Associate Professor and Canada Research Chair in Sustainable Infrastructure, Department of Civil and Resource Engineering, Dalhousie University, Canada.

* Corresponding Author, email: asadat@dal.ca

Abstract

This study investigates the compressive behavior of thermoset glass fiber-reinforced polymer (GFRP) bars across different grades, sizes, and length-to-diameter (L/d_b) ratios using a novel testing fixture. A total of 61 specimens were subjected to testing, encompassing bars in three sizes, three grades, and three L/d_b ratios. The new testing fixture, informed by insights from previous methods and initial investigations, easily adaptable to different bar diameters, and eliminates the need for resin, grout, or permanent attachment, allowing for reuse. Using this testing method, consistent measurements of compressive strengths were obtained for L/d_b=2, reaching approximately 0.86 of their average measured tensile strength. These measurements exhibited a low standard deviation (SD) of 0.047 and a low coefficient of variation (CoV) of 5.4%. Additionally, the elastic modulus in compression closely aligned with the tensile modulus, with a ratio of 0.97, and minimal variation in measurements (SD = 0.032 and CoV = 3.3%). Increasing L/d_b ratio of bars from 2 to 6 escalated result variability and reduced the compressive to tensile strength ratio (f_{fc}/f_{ft}) from 0.86 to 0.63, mainly due to increased susceptibility to buckling as observed in the experiments. However, the elastic modulus ratios (E_{fc}/E_{ft}) remained consistent around 1.0. Results of a comparative statistical analysis using data from studies over the past decade highlighted a decreasing trend in f_{fc}/f_{ft} ratios with increasing L/d_b ratios, having an average of 0.7. However, E_{fc}/E_{ft} remains stable at around 1.0 across different L/d_b ratios.

DOI: https://doi.org/10.1061/JCCOF2.CCENG-4971

Keywords: Compressive Properties; Strength; Elastic Modulus; GFRP Bars; Novel Fixture; Statistical Analysis

INTRODUCTION

While there is extensive literature on the compression behavior of polymer matrix fiber-reinforced materials, including GFRP, the mechanisms leading to compressive failure, particularly for GFRP bars, remain underexplored. This gap creates uncertainty about their contribution to GFRP-reinforced concrete (RC) columns' load-bearing capacity. Despite design guidelines in standards like ACI CODE-440.11-22 (ACI, 2022) and CSA S6-19 (CSA, 2019), the latest Canadian standard (CSA, 2021) assumes zero compressive strength and stiffness for FRP bars. This underscores the need for standardized methods to measure GFRP bars' compressive strength and modulus. Although progress has been made, a universally accepted standard, like that for tensile testing (ASTM, 2021), remains elusive. Addressing these challenges is essential for improving the integration of GFRP bars in structural design.

Prior studies have investigated the compressive mechanical properties of FRP bars. Wu's experiments and numerical simulations (Wu, 1991) scrutinized both smooth and ribbed FRP bars, revealing that the compressive strength and modulus hinged on bar dimensions and type. Similarly, Chaallal and Benmokrane (1993) explored various diameters of GFRP bars, affirming an ultimate compressive strength averaging approximately 77% of the tensile strength, while the elastic modulus was found comparable to the corresponding values in tension. Kobayashi and Fujisaki (1995) studied FRP bars embedded within concrete prisms, yielding compressive strengths within the range of 30% to 40% relative to their corresponding tensile strengths. Deitz et al. (2003) introduced a method in which GFRP bars were positioned at the center of threaded steel rods. They categorized non-slender GFRP bars' compressive strength into three groups: Crushing, Buckling, and a combination of Crushing and Buckling. Almerich-Chulia et al. (2012) and Bruun (2014) tested GFRP bars using a similar test method, with different L/d_b values of 11 and 5, respectively.

Both studies reported an average compressive strength equivalent to 60% of the tensile strength, while E_{fc}/E_{ft} was found to be around 1. By using the same methodology, Tavassoli et al. (2015) reported that the compressive strength of GFRP bars is approximately half of their ultimate tensile strength, and the elastic modulus in compression is comparable to that under tension. As seen, similar results from the same method indicate the effect of test method in the compressive to tensile strength ratio. Khan et al. (2015) investigated the load-extension and stress-strain behaviors of Carbon Fiber Reinforced Polymer (CFRP) and GFRP bars. In their proposed method a simplified version of the ASTM D695-10 (ASTM, 2010) compression test method for rigid plastics was used by replacing the hardened blocks with flat, parallel high-strength steel plates. Compressive strengths were found to hover at around 60% of their tensile counterparts, while E_{fc}/E_{ft} was around 75%.

More recent studies have proposed innovative test setups for investigating the compressive behavior of GFRP bars. Fillmore and Sadeghian (2018) employed hollow cylindrical steel caps filled with epoxy-based adhesive to encase the bar and the steel cylinder. The compressive strength of GFRP bars was seen to be approximately 67% of their tensile strength, while the compressive elastic modulus was found comparable to tensile. Khorramian and Sadeghian (2021) adopted a similar test apparatus, embedding GFRP bars within adhesive anchors complemented by steel caps at both extremities. In this setup, the f_{fc}/f_{ft} for GFRP bars averaged approximately 81%, while E_{fc}/E_{ft} was found to be around 1. AlAjarmeh et al. (2019) refined existing test procedures and employed hollow steel caps filled with cementitious grout to confine the top and bottom ends of the GFRP bars. They recommend an L/d_b of 8 as the most representative indicator of compressive strength and elastic modulus. In a more recent study by AlAjarmeh et al. (2022) the effects of elevated temperatures and varying slenderness ratios on the compressive behavior of GFRP bars were

investigated. Findings indicated a shift in failure mode from fiber-dominant to matrix-dominant at higher temperatures and from shear-crushing to buckling-splitting failure with an increase in slenderness ratio. D'Antino and Pisani (2023) studied the behavior of thermoset and thermoplastic GFRP bars using the set-up proposed by Khan et al. (Khan et al., 2015), Results showed f_{fc}/f_{ft} spanning from 55% to 82%, , while E_{fc}/E_{ft} in average is slightly under 1. Mirdarsoltany et al. (2023) Investigated the L/d_b and cutting method on the compressive strength of GFRP bars through introducing a test method. A steel centering fixture with a 3D-printed plastic plug was used to minimize load eccentricity effects. Micro-CT scans revealed that the majority of damage occurred after reaching 75% of ultimate strength. An experimental and statistical study by Bujotzek et al. (2024) confirmed the presumption of the elastic modulus in compression being equal to that in tension. The test method involved grouted anchor sleeves at both ends of the bars, with an L/d_b ratio of 6 for all tests. The highest f_{fc}/f_{ft} were observed for GFRP specimens (around 70%), followed by Basalt Fiber Reinforced Polymer (BFRP) and CFRP. Sadat Hosseini et al. (2024) investigated the impact of low axial loads on the behavior of GFRP-RC beams and sought to determine the compressive properties of #8 GFRP bars using an extended method based on the one developed by Khorramian and Sadeghian (2021). A gauge length of $2d_b$, was used and both ends of the bar were anchored in resin within large steel tubes.

Despite efforts to understand the behavior of GFRP bars under compression, discrepancies in findings persist, and a standardized testing method remains elusive. These uncertainties affect the reliability of compressive strength values and undermine confidence in codes and standards, often excluding GFRP bars from compression-based designs like columns. This study addresses these issues by improving previous methods and introducing a reusable testing fixture. Prior research by the authors (Sadat Hosseini & Sadeghian, 2023) highlighted limitations of existing methods,

particularly ASTM D695-15 (ASTM, 2015), which underestimated FRP bar strength due to premature end failures and lateral displacement. In contrast, the current study's fixture provides nearly pure axial compressive loading, showing minimal variability in compressive strength and elastic modulus. Statistical analyses further validate these findings, offering more consistent results compared to previous studies.

MATERIALS

The bars used in this study were all thermoset GFRP bars made of boron-free glass fibers and vinyl ester resin through a pultrusion manufacturing process by Pultrall Company. Three different bar numbers (#5, #6, and #8) were considered, and within each bar number category, three distinct grades were employed. Grade I corresponds to the bars whose minimum elastic modulus is 46 GPa, while Grades II and III exhibit higher minimum elasticity moduli, specifically 50 and 60 GPa, respectively. Since each grade of bar has its effective diameter, this study comprised a total of nine different effective diameters (Table 1). Figure 1 illustrates the cross-sectional area of the bar specimens. Sample bars were obtained from the manufacturer and then cut into the required lengths for testing. Table 2 presents some initial material properties of the bars that are conducted according to the ASTM standards. The values in the table are the average values that were obtained from tests on 5 specimens per grade of each bar number. As depicted in the table provided, it is evident that the fiber content across all specimens consistently hovers at approximately 85%. The variations in mechanical properties among different grades can be attributed to disparities in the inherent mechanical characteristics of the fibers and resin materials used.

EXPERIMENTAL PROGRAM

Fixture Development Process

In light of the diverse range of methods employed and those that have been suggested, the authors adopted an approach in which the studies on compressive strength initiated with the simplest test method, outlined in ASTM D695-15 (ASTM, 2015), that some researchers have used. To this aim, a total of fifteen test specimens were prepared from bar #5-grade II, each with varying L/d_b. As per the standard, the specimens' lengths for compressive strength measurements were mandated to be twice the diameter of the bar. Therefore, three groups with L/d_b of 2, 2.75, and 4, based on slenderness ratios of 8, 11, and 16 were considered. This multi-group approach facilitated a comprehensive examination and comparison of failure mechanisms, as well as the impact of the L/d_b on strength. These specimens were methodically positioned beneath the loading jack of a 2 MN universal testing machine, with meticulous alignment ensuring their central placement atop the support disk through the use of positioning marks. To eliminate the risk of inadvertent eccentricities, a spherical platen was affixed to the loading jack. The loading speed was uniformly set at 1.3 mm/min for all specimens, based on ASTM D695-15 (ASTM, 2015), with displacement measurements recorded at 0.1-second intervals through a data acquisition apparatus. A Linear Potentiometer (LP) was affixed to the loading jack to measure vertical displacements. Notably, all tests were executed concurrently, under identical conditions, to maintain consistency.

Results of these initial tests showed the occurrence of premature failure at the ends of some specimens. This localized failure can be attributed to stress concentration and the susceptibility of the end cross section to local splitting. Specimens displaying comparatively higher compressive strengths predominantly underwent longitudinal splitting as their primary mode of failure. With the exception of cases where premature failure occurred, all specimens exhibited a consistent

failure pattern, characterized by initiation at one end, as indicated by the sequential development of cracking and audible breakage during testing. As a result, the ultimate compressive strengths reached approximately half of the tensile strength value. Figure 2 provides an illustration of the simple test setup and the specimens after failure.

Recognizing that the ends of bars are particularly vulnerable to initiating failure due to the inherent non-homogeneity of the composite bar cross-section, simple clamps were used to address the mentioned issue. Two clamps, composed of high-strength steel, were securely fastened to both ends of the specimens using four bolts. These clamps covered a length of bar equivalent to $1d_b$. The central aperture in the fixture matched the bar's effective diameter. In the context of this test series, seven bar specimens of #5-grade II were specifically cut to possess an L/d_b of 4, and the fixture clamps were affixed to both ends of each specimen. Consequently, the gauge length for this test series equated to $2d_b$, which is equal to the test specimens in the last series. Following the attachment of the clamps, the alignment of the clamp ends with the bar ends underwent straightness examinations, a step that emerged as the most time-intensive aspect of the testing process. Importantly, the loading procedure and instrumentation employed in this series remained consistent with those employed in the initial series. In addition to the Linear Potentiometer (LP) fixed to the loading jack, another one was installed to record the lateral movements (Figure 3a).

Although. failures observed at both the top and bottom ends of the specimen, unlike what was observed in the initial tests, the clamps confined the specimen ends and prevented the spread of end failures to the entire bar specimen. These end failures manifested in the form of matrix cracking, aligning with our expectations. Following these initial end failures, the specimens continued to bear more load until they ultimately failed at their mid-length. The deformed shape of the bar in Figure 3b showcases the final collapse of the bar. Based on the results obtained from

seven specimens, the compressive strength values demonstrate a consistent pattern, with an average value of 0.7 of their tensile strength.

This method harbored a notable drawback: the potential for lateral relative displacement of the clamps (Figure 3b). Such displacement can introduce a bending moment in the specimen, yielding results that do not accurately represent the pure compressive strength of the specimens. A similar approach was adopted in prior studies by Deitz et al. (2003), Fillmore and Sadeghian (2018), Khorramian and Sadeghian (2021), and D'Antino and Pisani (2023), their specimens also experienced the same displacement as seen in some failed specimen illustrations.

To address this challenge and enhance the clamping process, a new fixture was devised, as illustrated in Figure 4. This fixture comprises two clamping components, each spanning a length of 100 mm to increase the friction between bar and clamps, firmly securing the bar in place using 16 bolts of size 12.7 mm (0.5 in). The gauge length can be adjusted to accommodate bars of different ranges in size. For bars of different sizes, customized clamps can be manufactured. Two vertical steel alignment rods are incorporated in the fixture to prevent lateral displacement. Steel plugs are used inside the clamping objects to adjust the clamping length of the specimens. The top of the steel bar was completely flush with the top faces of the clamp when loading was applied, ensuring that the load was distributed evenly over the entire surface of the fixture. This configuration prevents any significant friction between the steel bars and the clamps from coming into effect.

The main idea behind this fixture comes from the standard test method provided in ASTM D6641 (ASTM, 2016). The process of applying load consists of a combined end- and shear-loading. The end loading is applied to the end edges of the specimen while the shear loading is applied through friction force on the GFRP specimen.

Main Tests and Results

The bar specimens employed in the tests using the proposed fixture featured a length of $6d_b$, with a gauge length of $2d_b$ to avoid any buckling effects, and a clamping length of $2d_b$ within each clamp. Each specimen was cut from a longer rebar, and both ends were carefully flattened using a milling machine. This process ensured that the bar ends were parallel within a tolerance of 0.025 mm in a plane perpendicular to the longitudinal axis of the bar. To safeguard the bar's surface from potential damage due to clamping forces, a combination of one-two layers of electrical tape and one layer of duct tape (constructed from polyethylene-coated cloth with a rubber resin adhesive) was applied to cover the clamped area of the specimens. Furthermore, at both ends of the bar specimens, two smooth steel plugs of matching diameter were positioned. The clamping force, applied through high-strength bolts of size 12.7 mm (0.5 in), was carefully calibrated for each bar size after conducting some preliminary tests without strain gauging (Sadat Hosseini & Sadeghian, 2024). To ensure uniform load distribution within the fixture, all bolts were tightened using a digital torque wrench to approximately 35 N-m for bar #5, 40 N-m for bar #6, and 50 N-m for bar #8. The selected values were tested without strain gauges as part of the calibration process to prevent potential damage to the bars and preserve the integrity of the fixture during testing. Figure 5 illustrates the specimen preparation, clamping, and testing process.

The bar specimen was positioned in the fixture under a 2 MN Instron testing machine, with a spherical platen attached to the loading jack to prevent eccentricities. All specimens were tested at a uniform loading speed of 1.3 mm/min, following the ASTM standard for rigid plastics (ASTM, 2015), with displacement recorded every 0.1 seconds. Tests were conducted simultaneously under consistent conditions. High-strength vertical steel rods ensured the fixture remained vertical, verified by a digital inclinometer with ±0.2° accuracy.

Figure 6 illustrates the sample failures observed in the specimens. As depicted, the predominant modes of failure in the bars were longitudinal splitting and subsequent horizontal crushing, following the longitudinal splitting. Notably, thinner bars (5 and #6) of Grade I primarily exhibited horizontal crushing as their mode of failure. In instances where a specimen experienced a longitudinal splitting failure, discernible drops in the loading diagram were evident. Furthermore, certain specimens exhibited localized failures within the fixture due to direct pressure exerted by the steel plugs within the fixture. This resulted in observable dips in the load-displacement diagrams before reaching the peak load during these tests and displacements up to 8 mm.

An examination of failure modes was conducted, identifying three primary modes as outlined by Hahn and Williams (1984). The first, longitudinal splitting, arises from transverse tension failure of the polymer matrix due to the mismatch in Poisson's ratios between the fibers and the matrix. In this study, longitudinal splitting was the dominant failure mode for GFRP bars with a vinyl ester matrix (Figure 7). The second mode, shear crippling and fiber kinking, involves localized shear deformation and cross-sectional distortion due to the formation of shear bands (Figure 8). These bands are likely initiated by small deviations from straightness in the test fixture, as the fibers were straight during production. This mode, seen after horizontal crushing from fiber compressive failure and matrix cracking, begins with individual fiber failure and progressively leads to the failure of adjacent fibers. Shear crippling is more prevalent in low-strain fibers like carbon, but for glass fibers, longitudinal splitting and horizontal crushing were the primary modes of failure (Figure 9). These findings suggest that the stiffness of the matrix and test setup play significant roles in determining the failure mechanism.

Figures 10 and 11 show load versus stroke displacement, and axial stress versus average axial strain curves of compression tests, respectively. The applied load – stroke displacements curves

(Figure 10) show an approximately linear behavior of the bars in compression, with limited scatter and insignificant drops in before the peak load. Since the specimen is under direct compressive force at both ends as well, these drops are due to local failures in the specimens ends. All the specimens failed due to sudden crushing at their peak load. The peak load for each specimen was divided by the nominal cross-sectional area of bars to calculate the compressive strength of bars. The load-displacement diagrams give a general indication of when damage initiates. However, because the total displacement includes contributions from various sources, such as clamping and actuator movement, the stroke displacement alone cannot be used to assess the stiffness of the bars. The actual deformation of the FRP bars within the gauge length is minimal compared to the overall stroke displacement. Therefore, strain gauges were applied directly to the bars to isolate and accurately measure their strain and calculate the elastic modulus from the strains.

In the stress-strain diagram (Figure 11) linear behavior of the bars in compression is observed. Since there is not a standard for calculating the compressive chord modulus of elasticity of the bars, the elasticity moduli were calculated using the methodology provided by ASTM 7205M (ASTM, 2021) for tensile testing of bars using stresses at the strain of 0.001 and 0.003. As shown in Figure 11, the stress-strain relationships for each specimen type are consistent. Errors from issues like improper strain gauge attachment or wire connection were corrected by repeating tests and substituting accurate results. Peak stresses, marked by × in Figure 11, were reached with mostly linear strain recordings, with minimal nonlinear behavior or strain gauge failure in some cases. Almost all specimens reached a strain of 0.015, with 0.02 appearing as the nominal maximum strain, except for bar #8, which had lower compressive strains. Post-peak strain values were removed for clarity, as they offered no additional insight.

To compare the results of the tests on the compressive behavior of the bars, results of the tensile tests, conducted by the manufacturer, such as ultimate tensile strength, tensile elastic modulus, and ultimate tensile strain are presented in Table 3. As seen, the values of the CoV are lower than 10%, indicating that the data points are relatively close to the mean. To validate the manufacturer's specifications, a series of tensile tests were performed on five specimens of #5 (15M) Grade II bars according to ASTM D7205-21 (ASTM, 2021) and CSA S806:12 (R21) (CSA, 2021). Each specimen measured 1.76 meters in total length, with anchors of 550 mm each. The free gauge length between the steel pipe anchors for the GFRP bar was 660 mm, with two strain gauges affixed at the midpoint. Figure 12 illustrates the setup of the tensile test along with a failed specimen, while Figure 13 shows the relationship between tensile load and stroke displacement, as well as tensile stress and average axial strain. The results revealed an average tensile strength of 1020 MPa, with an SD of 25 MPa and a CoV of 2%. Comparison of the test outcomes with the manufacturer's specifications (refer to Table 3) indicates a close alignment between the two datasets. Consequently, the data from Table 3 was utilized to compare the findings of this study regarding compressive behavior with the observed tensile characteristics.

Table 4 presents the quantitative results of the compression tests using the proposed fixture. Also, the results were compared against the tensile characteristics to provide a better understanding of the ratio of f_{fc}/f_{ft}, E_{fc}/E_{ft}, and compressive to tensile ultimate strain ($\varepsilon_{fcu}/\varepsilon_{ftu}$). As seen, the ratios of the strengths are consistently around the overall average of 86 percent with an SD of 0.047 and CoV of 5.4%. The average ratio of strength in these tests is relatively higher than those presented in previous research. This can be attributed to modifications made during testing, particularly the proposed fixture, which prevents lateral displacement. Lateral displacement can introduce shear and flexural stresses, leading to unrealistically low compressive strength values, as shear and

flexural strengths are lower than compressive and tensile strengths. Variations in results may also stem from sand coating and surface unevenness from manufacturing, causing uneven stress distribution. These variations are realistic, as they reflect conditions encountered in practice. In some cases, f_{fc}/f_{ft} exceeds 1, likely due to smoother, more consistent bar surfaces, which halt lateral crack propagation by ensuring more uniform compression.

The E_{fc}/E_{ft} are also consistent, showing an average of 0.97, an SD of 0.032 and a CoV of 3.3%. This shows that the elastic modulus of the GFRP bars in compression is approximately equal to their tensile elastic modulus. In several cases, ratios exceeding 1 were observed, likely due to the resin type, and processing methods. The other important factor in the compressive behavior of the bars is their ultimate compressive strain. The ultimate compressive strains are selected as the ultimate point that the strain gauge readings were still linear or close to linear before the sudden drop in the strength due to crushing. The SD of 0.045 and a CoV of 5.3%, show that the results were relatively consistent.

Effect of Length-To-Diameter Ratio

The fixture as mentioned is adjustable for testing longer bars. Longer steel alignment rods were used as support for the fixture to accommodate longer lengths of the GFRP bar specimens. The effect of higher L/d_b ratios were investigated by testing bars L/d_b ratios of 4 and 6. Eight tests per each ratio and a total of 16 tests were conducted and results of these experiments such as load-displacement curves and stress-strain curves were collected and analyzed. By having the results of the tests on L/d_b=2 in the last section, a sensitivity analysis was conducted for the effect of L/d_b. Specimens for this set of experiments were #5 (15M) bars of Grade II, and the process of specimen preparation, placement in the fixture, and testing followed the one explained before.

Figure 14 illustrates the deformation of the test specimens monitored during the tests on bar specimens with L/d_b of 4 and 6. In Figure 14a, the bar specimens experienced lateral deformation near the mid-length, leading to failure at either the top or bottom end. The deformation is more pronounced in Figure 14b for the bar specimens with an L/d_b=6, where the bars deform into a curved shape due to compressive forces. This deformation introduces additional moments on the specimen, causing failures at one or both ends as shown under relatively lower loads.

Figure 15 presents load-displacement and stress-strain behaviors of GFRP bars with L/d_b=4 and L/d_b=6 under compressive loads. Out of the eight specimens tested for each L/d_b group, five were selected for Figure 15. The selection was based on ensuring that all modes of failure were represented while maintaining consistency with the number of diagrams shown for L/d_b = 2 and avoiding overcrowding of diagrams or confusion in the presentation. In Figure 15a (L/d_b=4), the axial load increases linearly with stroke displacement, indicating elastic behavior, with a maximum load of approximately 195 kN in Test 5. Figure 15b (L/d_b=6) also shows linear elastic behavior, but the peak load is slightly lower, around 160 kN in Test 1, suggesting greater sensitivity to imperfections. The stress-strain behaviors for L/d_b=4 (Figure 15a) show consistent strains at failure, with peak stresses calculated from the load-displacement curves. For L/d_b=6 (Figure 15b), the initial stress-strain relationship is similarly linear, but the peak stress is slightly lower, with more variability in failure strains.

Table 5 presents the results for the compressive strength and elastic modulus. The average ratio of f_{fc}/f_{ft} is 0.78 for bars with an L/d_b ratio of 4, which is higher than the 0.63 observed for bars with an L/d_b ratio of 6. This shows that the shorter bars have a higher compressive strength relative to their tensile strength. The SD for the L/d_b=4 bars is 0.05, while it is 0.09 for the L/d_b=6 bars,

indicating more variability in the ratio for the slender bars. The CoV is 7% for the L/d_b=4 bars and 15% for the L/d_b=6 bars, indicating a more consistent ratio in the shorter bars.

The average ratio of E_c/E_t is 0.94 for bars with L/d_b=4 and 0.92 for bars with L/d_b=6, indicating very similar behavior in terms of stiffness in both compression and tension for both sets of bars. The SD is 0.06 for the L/d_b=4 bars and 0.07 for the L/d_b=6 bars, indicating slightly more variability in the ratio for the slender bars. The CoV is 7% for the L/d_b=4 bars and 8% for the L/d_b=6 bars, showing a slightly higher variability for the bars with a higher L/d_b ratio.

Figure 16 depicts the relationship between the ratios of f_{fc}/f_{ft} and E_c/E_t with varying L/d_b ratios of 2, 4, and 6 for GFRP bars. The ratio f_{fc}/f_{ft}, shown by circles, demonstrates a clear decreasing trend as the L/d_b ratio increases. This trend is captured by three quadratic regression equations as shown in the figure. The equation corresponding to the middle curve was fit on the mean values accompanying error bars. These error bars represent SDs, representing the fluctuation in f_{fc}/f_{ft}, and indicating that L/d_b=6 has more variation. However, the other two fit on average ± one SD as the lower and upper bonds. These equations suggest that as the GFRP bars become more slender (higher L/d_b ratio), f_{fc}/f_{ft} diminishes. Specifically, the data points indicate a decline in the ratio from around 0.86 for L/d_b=2 to approximately 0.63 for L/d_b=6. This behavior is consistent with the increased susceptibility of slender bars to buckling under compressive loads, which adversely affects their effective compressive strength.

In contrast to f_{fc}/f_{ft}, the ratio E_c/E_t remains relatively stable across different L/d_b ratios. The average value of E_c/E_t is approximately 0.93, with minimal variation, as depicted by the squares and accompanying error bars. These error bars represent SDs, which show that the fluctuation in E_c/E_t is minor, indicating that the elastic properties of the material in compression and tension are consistent regardless of the bar's slenderness.

COMPARATIVE STATISTICAL ANALYSIS

In this section, findings from studies conducted over the past decade are compared with the outcomes of the current research. Selecting these recent studies ensures a fair comparison, as advancements in manufacturing technology and material quality have improved in recent years.

Figure 17 consists of two diagrams which compare the findings of this study with those of previous studies in the literature for the ratio of f_{fc}/f_{ft} and E_{fc}/E_{ft} of GFRP bars. The horizontal axis in both diagrams shows the L/d_b ratio of the bar specimens. According to Figure 17a, the data points from this study, represented by circles, are predominantly concentrated around a f_{fc}/f_{ft} ratio of approximately 0.8 to 1.0 for L/d_b ratios of 2 and 4, and about 0.6 for L/d_b=6. Comparing these findings with other studies, results of Bujotzek et al. (2024) exhibits a close average value of f_{fc}/f_{ft} to the findings of this study for L/d_b=6. D'Antino and Pisani (2023), cluster around L/d_b=4 showing slightly lower f_{fc}/f_{ft} values in average compared to this study which mostly can be attributed to their test setup using anchor sleeves with no restriction against lateral movement of the bars. Meanwhile, the data from Khorramian and Sadeghian (Khorramian & Sadeghian, 2021) display more variation in L/d_b=2, with values generally within the range of 0.55 to 1.0. The studies by Abed et al. (2020), and Fillmore and Sadeghian (2018) show approximately similar ratio of around 0.7 for L/d_b=2. AlAjarmeh et al. (2019) covered a wider range of L/d_b in their tests, from 2 to 16. They suggested that L/d_b=8 is the most representative value for the compressive strength and elastic modulus based on the observed trend of data in their tests and those by Deitz (2003) and Bruun (2014). However, Tavassoli et al. (2015) tested specimens with L/d_b=2, 6.4, and 10.8 and their test results on two bar types indicated a decreasing trend in f_{fc}/f_{ft} with increasing L/d_b, which is compatible with the average ratio of 0.56 reported at L/d_b=6 (Bujotzek et al., 2024).

Figure 17b presents the ratio of E_{fc}/E_{ft} against L/d_b. In this diagram, the data points from this study are mostly concentrated around an E_{fc}/E_{ft} ratio of 1.0 as also seen in Figure 16. Comparing these findings with other studies, it is seen that Sadat Hosseini et al. (2024), Khoramian and Sadeghian (2019), AlAjarmeh et al. (2019), and Fillmore and Sadeghian (2018) reported average ratios higher than 1.0 for L/d_b=2. For L/d_b=4, D'Antino and Pisani (2023) and AlAjarmeh et al. (2019) reported an average ratio of higher than 1 again. For L/d_b=6, Bujotzek et al. (2024) shows similar E_{fc}/E_{ft} ratios, closely matching the other studies, while Tavassoli et al. (Tavassoli et al., 2015) shows an average ratio of slightly less than 1 for L/d_b=6.4. Higher values of L/d_b, tested by AlAjarmeh et al. (2019) and Tavassoli et al. (2015) show equal and higher elasticity ratios than 1. Overall, considering the collective findings across all studies depicted in this figure, the ratio of E_{fc}/E_{ft} remains consistently close to 1, irrespective of the L/d_b ratio. This uniformity can primarily be attributed to the early stages of loading measurements, during which no damage or geometric effects such as buckling have emerged yet.

Figure 18 presents an analysis of strength ratio relationship with L/d_b ratio based on the overall collected data. Each data point for a given L/d_b is represented with a distinct marker symbol, while the average value for each L/d_b is illustrated with a thick dashed marker. A polynomial curve is fitted to these average values, as well as to the average values ± one SD, to capture the trend and variability within the data. The fitted polynomial curve indicates a descending trend, reflecting the general behavior of the average f_{fc}/f_{ft} values as L/d_b increases. This descending trend suggests that f_{fc}/f_{ft} tends to decrease with larger L/d_b ratios. Additionally, the data points at L/d_b=4 and L/d_b=8 show noteworthy higher values, marked by a large oval around. The higher strength ratios at these L/d_b values correspond to #3 bars, as observed in tests by (AlAjarmeh et al., 2019). Smaller diameter bars, such as #3, tend to exhibit higher compressive strengths due to reduced fiber

buckling, resulting in more uniform behavior. The failure modes in these bars showed less pronounced buckling compared to larger bars, which explains the elevated strength ratios. Although #3 bars are not commonly used as compression bars in structural elements, further investigation and additional testing for this bar size are recommended.

Figure 19 presents interval graphs to visualize and compare the ratios of f_{fc}/f_{ft} and E_{fc}/E_{ft} from this study with those of previous ones. The horizontal axis categorizes the different studies, while the vertical axis displays the respective ratios. Each central point represents the average value, with error bars indicating the 95% confidence intervals calculated from individual SDs. The data points for f_{fc}/f_{ft}, depicted by circles, show a range of variability among the different studies. This study, represented as group 1, demonstrates relatively narrow confidence intervals, indicating less scatter and more consistent data compared to the other studies which considered various L/d_b ratios. For E_{fc}/E_{ft}, represented by squares, the data from this study shows narrow confidence intervals.

The histograms in Figure 20 illustrate the distribution of f_{fc}/f_{ft} and E_{fc}/E_{ft}. Figure 20a shows that the mean ratio of f_{fc}/f_{ft} is almost 0.70 with an SD of around 0.17. The distribution is approximately normal but slightly skewed to the right, indicating that the majority of data points are clustered around the mean, with a gradual tapering off towards higher values. This suggests that, on average, the experimental compressive strength of the GFRP bars is about 70% of the nominal strength, pointing to a consistent underperformance in compressive strength compared to the expected nominal values. The moderate spread indicated by the SD highlights some variability in the results, which could be attributed to inconsistencies in the test methods, type of fixture used, material properties and manufacturing process.

In contrast, Figure 20b reveals that the mean ratio of E_{fc}/E_{ft} is very close to 1.0 with an SD of 0.07. This distribution is symmetrical and closely approximates a normal distribution, with most data

points tightly clustered around the mean. The near-unity mean value suggests that the experimental elastic modulus in compression is very close to the tensile modulus, indicating that the GFRP bars perform similarly in compression and tension in terms of stiffness. The low SD reflects high consistency and reliability in the measured elastic modulus regardless of test method and L/d_b ratio.

Table 6 and Table 7 present the ANOVA results comparing f_{fc}/f_{ft} and E_{fc}/E_{ft} ratios, respectively, between this study and combined results from other studies (numbered 2 to 6 in Figure 19). For f_{fc}/f_{ft}, this study shows an average ratio of 0.8328 with a variance of 0.0069, while other studies have an average of 0.6604 and a variance of 0.0283. The F-value of 10.6751 and P-value of 0.0021 indicate statistically significant differences. Similarly, for E_{fc}/E_{ft}, this study's average is 0.9661 with a variance of 0.0011, compared to 1.0180 and 0.0057 for other studies. The F-value of 4.8587 and P-value of 0.0326 show significant differences, though the variation in E_{fc}/E_{ft} is smaller, suggesting greater consistency across studies.

DISCUSSION

As reviewed in this paper, several studies aimed to measure the compressive characteristics, particularly the compressive strength, of FRP bars by either utilizing the existing methods, which are not specifically proposed for FRP bars, or proposing new methods. The ASTM D695-15 (ASTM, 2015) test method, commonly utilized for determining the mechanical properties of rigid plastics, including both reinforced and unreinforced materials, has been used before for FRP bars (Khan et al., 2015). It exhibits noteworthy limitations when used for FRP bars. One limitation pertains to the necessity of conducting the test at relatively low and uniform rates of loading. While this requirement poses minimal concerns when evaluating bars for standard structural applications, another significant limitation becomes evident when assessing the elastic modulus. Specifically, the ASTM test method is only applicable to composites with an elastic modulus equal to or less

than 41,370 MPa. Given that manufacturers of GFRP bars often produce products with mechanical properties, particularly elasticity moduli, exceeding 40 GPa, it becomes apparent that this test method may not be suitable for bars boasting elasticity moduli surpassing 50 GPa. The other main concern is the susceptibility of the bar ends to premature failure due to the nonhomogeneous cross section at the ends of the specimen. The findings of the authors demonstrated that achieving f_{fc}/f_{ft} ratios exceeding 50% is a relatively rare occurrence when utilizing the ASTM D695-15 (ASTM, 2015) test method.

Other methods consist of embedding the bars in concrete prisms (Kobayashi & Fujisaki, 1995) or in threaded rods by Deitz et al. (2003). This idea then utilized and further developed by other researchers such as Fillmore and Sadeghian (2018) and Khorramian and Sadeghian (2018) Similar ideas of using two hollow cylindrical steel, caped with a steel plate from one end, and filling the gap between bar and cylinder with high-strength epoxy-based adhesive were investigated. Later, AlAjarmeh et al. (2019) further modified the previous ideas (Fillmore & Sadeghian, 2018; Khorramian & Sadeghian, 2021) by removing the sealed ends to make the procedure reusable. All these studies mainly followed the idea of ASTM D7205 (ASTM, 2021) by fixing the bar in a resin media. In another study by the authors (Sadat Hosseini & Sadeghian, 2024), the idea of removing the sealed ends was examined. However, this methodology was examined by the authors for #8 bars (Hosseini et al., 2024) and since the epoxy sticks hard to the internal wall of the steel tube, and it cannot be easily removed.

The proposed fixture in this study has a straightforward method of using reusable steel clamps and an intervening elastic material between clamps and bar. The adjustment of the bar inside the clamp is important and equal specific torque is used for all bolts to make sure the clamping force is evenly distributed. Results for L/d_b=2 showed a relatively higher and more consistent compressive

strength indicating that the material properties of the bars in compression should not be neglected. Further analysis was conducted for L/d_b=4 and 6 to provide more information and insight on the longer test specimens. It was seen that the strength of rebar specimen decreases by increasing L/d_b due to geometric effects such as buckling, but E_{fc}/E_{ft} remains approximately constant around 1.

Comparing the results of the present study with AlAjarmeh et al. (2019) shows that both studies collectively highlight the significant impact of the L/d_b on the compressive behavior of GFRP bars, though they present some differing trends. The present study shows a clear decrease in the ratio of f_{fc}/f_{ft} from 0.86 for L/d_b=2 to 0.63 for L/d_b=6. This suggests that as the bars become slenderer, their compressive strength relative to tensile strength diminishes, likely due to increased susceptibility to buckling under compressive loads. In contrast, AlAjarmeh et al. (2019) report that for bar numbers #3, #5, and #6, the increase in slenderness ratio from 2 to 16 changes the failure mode from crushing to buckling, but they also show a trend where f_{fc}/f_{ft} initially increases with the L/d_b ratio from 2 to 8 before decreasing at higher ratios. This discrepancy suggests that for lower L/d_b ratios (up to 6), the compressive strength relative to tensile strength might improve slightly due to changes in failure modes and the geometric properties of the bars. Additionally, both studies agree that beyond a certain L/d_b ratio, buckling becomes the dominant failure mode, leading to a reduction in compressive strength. AlAjarmeh et al. (2019) found that bars with an L/d_b ratio of 8 exhibited consistent failure behavior and the highest f_{fc} values among the tested bars, which was not observed in the present study as it did not investigate L/d_b ratios beyond 6. Moreover, the present study found that E_{fc}/E_{ft} remains relatively stable across different L/d_b ratios, indicating consistent elastic properties. AlAjarmeh et al. (2019) similarly noted that E_{fc} is not significantly influenced by the slenderness ratio.

The collected database by Bujotzek et al. (2024) showed a decrease in scatter for both compressive strength and elastic modulus when slenderness increased. However, it is pertinent to note that this decrease in scatter may also stem from the comparatively fewer tests conducted at higher L/d_b ratios which suggests further investigations. Through comprehensive analysis, Bujotzek et al. (2024) observed that the relationship between f_{fc}/f_{ft} and L/d_b follows an inverted parabolic trajectory, peaking at L/d_b=8, as also suggested by AlAjarmeh et al. (2019). In the present study, the average values of f_{fc}/f_{ft} at each L/d_b were calculated followed by curve fitting. The resultant curve resembled an inverted parabola, akin to previous studies, albeit with a consistent declining trend observed with increasing L/d_b ratios.

By comparing the results of this study with recent literature, a range of 50 to 100 percent for the f_{fc}/f_{ft} ratio was observed, with differences attributed to factors such as specimen slenderness, material properties, manufacturing process, and testing method. In FRP-RC design, compressive strength is just one material property, while bar buckling between lateral supports, a geometric issue, also significantly limits compressive capacity. Large-scale tests on FRP-RC members can investigate these factors, allowing for observation of failure modes and inform design improvements.

The test results, obtained in a controlled setup, may differ from the behavior of FRP bars in real-world columns due to factors like boundary conditions and lateral support. To address this, applying reduction factors, similar to those used for concrete and FRP bars in tension, is necessary for design to account for these uncertainties. The f_{fc}/f_{ft} ratio provides an upper bound for FRP bar behavior and could serve as a basis for future reduction factor development in design practices.

CONCLUSIONS

The compressive behavior of thermoset GFRP bars was investigated across various grades, sizes, and length-to-diameter ratios. The study proposed a novel testing fixture with enhanced configuration and functionality to measure compressive strength and elastic modulus measurements. The core findings of the present research are as follows:

- The compressive strength of GFRP bars from the proposed test method for L/d_b ratio of 2 exhibited an average of approximately 0.86 of their tensile strength with an SD of 0.047 and CoV of 5.4%. Moreover, the elastic modulus in compression closely aligned with the tensile modulus of these bars, showing a ratio of 97% with an SD of 0.032 and CoV of 3.3%, which confirms the findings in the literature.
- Almost all specimens exceeded a strain of 0.015, which can be considered the maximum compressive strain for the bars. However, 0.02 can be taken as the nominal maximum strain, as most peak stresses were extrapolated around this value, except for bar #8, which showed slightly lower maximum strains.
- Increasing L/d_b from 2 to 6 leads to a decrease in the ratio of f_{fc}/f_{ft} from 0.86 to 0.63, indicating the geometry effects on the strength rather than pure material properties. While E_{fc}/E_{ft} remained stable around 1. Slenderer bars exhibited greater variability in compressive strength and were more prone to buckling. The results regarding the effect of L/d_b are based on tests on #5 (15M) bars of Grade II.
- A comparison of f_{fc}/f_{ft} and E_{fc}/E_{ft} ratios in this study with recent research in the field was conducted. A close agreement was seen for L/d_b=6, while diverging from other for L/d_b=4 due to differences in test setups and higher compressive strengths of smaller bar sizes (such as #3) due to less susceptibility to buckling. Additionally, analysis on all data sets suggests

a decreasing trend in strength ratios with increasing L/d_b ratios, as evidenced by the polynomial curve fitted to the data, aligning with the findings of this research.

- When considering all available data, average values of 0.7 and 1.0 were observed for f_{fc}/f_{ft} and E_{fc}/E_{ft} ratios, respectively. This underscores the significance of acknowledging the compressive properties of GFRP bars. The higher variance in f_{fc}/f_{ft} ratios across studies indicates greater scatter in the overall data, whereas E_{fc}/E_{ft} ratios demonstrate higher consistency. The moderate spread in f_{fc}/f_{ft} ratios may stem from inconsistencies in test methodologies, fixture types, differences in failure modes of various bar sizes, and material properties, highlighting the importance of future investigations particularly for high L/d_b ratios and a standardized testing protocols to ensure accurate and reliable results.
- Precise specimen clamping is crucial in the proposed experimental setup to avoid issues like excessive force causing localized pre-test failures or inadequate clamping leading to bar slippage and premature failures. To prevent damage to the bar's surface due to tightening, elastic tapes were employed as intervening materials. Meanwhile using robust fabric materials, such as CFRP fabric on smaller bar diameters yielded consistent results.
- As manufacturing quality continues to advance, the proposed fixture holds promise for achieving more consistent results in future implementations. This study focused on analyzing the three most frequently used bar sizes in practical applications. All bars utilized in this study were sand coated. As a potential avenue for future research, exploring additional bar sizes, higher L/d_b ratios, other surface finish, and various types of FRP materials could provide a comprehensive assessment of their compressive properties using the established fixture. In this study, a uniform displacement rate was used to simulate real conditions for GFRP bars in columns. Future studies can consider a constant strain rate to

further explore their compressive behavior. Furthermore, the use of reduction factors for FRP bars under compression is recommended, and further reliability analysis is suggested to bridge the gap between test results and practical applications.

DATA AVAILABILITY STATEMENT

The data that support the findings of this study are available from the corresponding author upon reasonable request.

ACKNOWLEDGEMENTS

We sincerely thank PULTRALL Inc. for providing the V-ROD composite bars and tensile test results used in this study. Special thanks to Dean Grijm, Lab Technician at Dalhousie University, for his crucial role in manufacturing the fixture, and to our research group members, Alireza Jafari, Ali Alinejad, and Raghad Kassab, for their invaluable assistance during testing.

REFERENCES

Abed, F., Mehaini, Z., Oucif, C., Abdul–Latif, A., & Baleh, R. (2020). Quasi-static and dynamic response of GFRP and BFRP bars under compression. *Composites Part C: Open Access*, *2*, 100034.

ACI. (2022). *ACI CODE-440.11-22: Building Code Requirements for Structural Concrete Reinforced with Glass Fiber-Reinforced Polymer (GFRP) Bars-Code and Commentary*. American Concrete Institute.

AlAjarmeh, O., Manalo, A., Benmokrane, B., Schubel, P., Zeng, X., Ahmad, A., Hassanli, R., & Sorbello, C.-D. (2022). Compression behavior of GFRP bars under elevated In-Service temperatures. *Construction and Building Materials*, *314*, 125675.

AlAjarmeh, O. S., Manalo, A. C., Benmokrane, B., Vijay, P. V, Ferdous, W., & Mendis, P. (2019). Novel testing and characterization of GFRP bars in compression. *Construction and Building Materials*, *225*, 1112–1126.

Almerich-Chuliá, A., Martin-Concepcion, P., Molines-Cano, J. M., & Rovira-Soler, J. (2012). Innovative Design of GFRP Bars for Concrete Structures. *Advanced Materials Research*, *457*, 553–556.

ASTM. (2010). *ASTM D695 − 10, Standard Test Method for Compressive Properties of Rigid Plastics*.

ASTM. (2014). *ASTM E1356-08(2014), Standard Test Method for Assignment of the Glass Transition Temperatures by Differential Scanning Calorimetry*.

ASTM. (2015). *ASTM D695 − 15, Standard Test Method for Compressive Properties of Rigid Plastics*. American Society for Testing and Materials.

ASTM. (2016). *ASTM D6641/D6641M − 16, Standard Test Method for Compressive Properties of Polymer Matrix Composite Materials Using a Combined Loading Compression (CLC) Test Fixture*. American Society for Testing and Materials.

ASTM. (2018). *ASTM D2584 − 18, Standard Test Method for Ignition Loss of Cured Reinforced Resins*.

ASTM. (2021). *ASTM D7205/D7205M, Standard Test Method for Tensile Properties of Fiber-Reinforced Polymer Matrix Composite Bars*.

ASTM. (2022). *ASTM D570 − 22, Standard Test Method for Water Absorption of Plastics*.

Bruun, E. (2014). GFRP bars in structural design: determining the compressive strength versus unbraced length interaction curve. *Journal of Student Science and Technology*, *7*(1).

Bujotzek, L., Beck, D., Apostolidi, E., & Waldmann, D. (2024). Experimental and statistical investigations of the material properties of FRP reinforcement in compression. *Construction and Building Materials*, *414*, 134782.

Chaallal, O., & Benmokrane, B. (1993). Physical and mechanical performance of an innovative glass-fiber-reinforced plastic rod for concrete and grouted anchorages. *Canadian Journal of Civil Engineering*, *20*(2), 254–268.

CSA. (2019). *S6:19 - Canadian Highway Bridge Design Code*. Canadian Standards Association.

CSA. (2021). *S806:12(R21) - Design and construction of building structures with fibre-reinforced polymers*. Canadian Standards Association.

D'Antino, T., & Pisani, M. A. (2023). Tensile and compressive behavior of thermoset and thermoplastic GFRP bars. *Construction and Building Materials*, *366*, 130104.

Deitz, D. H., Harik, I. E., & Gesund, H. (2003). Physical properties of glass fiber-reinforced polymer rebars in compression. *Journal of Composites for Construction*, *7*(4), 363–366.

Fillmore, B., & Sadeghian, P. (2018). Contribution of longitudinal glass fiber-reinforced polymer bars in concrete cylinders under axial compression. *Canadian Journal of Civil Engineering*, *45*(6), 458–468.

Galen L.L.C. 2017. TEST REPORT №K.386 -17.B.AKS-6. National Research Moscow State University of Civil Engineering, Moskau.

Hahn, H. T., & Williams, J. G. (1984). Compression failure mechanisms in unidirectional composites. *ASTM Symp. on Composite Mater.*, *NAS 1.15: 85834*.

Hosseini, A. S., Velkumar, S. K., & Sadeghian, P. (2024). Behavior of GFRP-Reinforced Concrete Members under Combined Bending Moment and Low Axial Load. *Journal of Composites for Construction*, *28*(4), 04024025.

Khan, Q. S., Sheikh, M. Neaz. & Hadi, M. N. S. (2015). Tension and compression testing of fibre reinforced polymer (FRP) bars. In Z. Wu, G. Wu & X. Wang (Eds.), Joint Conference of the 12th International Symposium on Fiber Reinforced Polymers for Reinforced Concrete Structures (FRPRCS-12) & the 5th Asia-Pacific Conference on Fiber Reinforced Polymers in Structures (APFIS-2015) (pp. 1-6).

Khorramian, K., & Sadeghian, P. (2018). “New testing method of GFRP bars in compression.” In Proc., Canadian Society for Civil Engineering Annual Conf., Fredericton, NB, Canada, June 13–16.

Khorramian, K., & Sadeghian, P. (2021). Material characterization of GFRP bars in compression using a new test method. *Journal of Testing and Evaluation*, *49*(2), 1037–1052.

Kobayashi, K., & Fujisaki, T. (1995). 32 compressive behavior of FRP reinforcement in non-prestressed concrete members. *Non-Metallic (FRP) Reinforcement for Concrete Structures: Proceedings of the Second International RILEM Symposium*, *29*, 267.

Mirdarsoltany, M., Roghani, H., Masoule, M. S. T., Khodadadi, N., Ghahremaninezhad, A., & Nanni, A. (2023). Evaluating GFRP bars under axial compression and quantifying load-damage correlation. *Construction and Building Materials*, *409*, 133945.

Sadat Hosseini, A., & Sadeghian, P. (2023). Experimental and Comparative Study on Compressive Strength of GFRP Rebars. In: Desjardins, S., Poitras, G.J., El Damatty, A., Elshaer, A. (eds) *Proceedings of the Canadian Society for Civil Engineering Annual Conference 2023*, Volume 13. CSCE 2023. Lecture Notes in Civil Engineering, vol 507. Springer, Cham. https://doi.org/10.1007/978-3-031-61539-9_12

Sadat Hosseini, A., & Sadeghian, P. (2024). An Effective Simple Fixture for Testing GFRP Rebars in Compression. *SP-360: Proceedings of the 16th International Symposium on Fiber-Reinforced Polymer (FRP) Reinforcement for Concrete Structures (FRPRCS-16)*, 225–241, Sponsored by ACI Committee 440, ACI Concrete Convention, March 24-28, 2024, New Orleans, LA, USA, DOI: 10.14359/51740627.

Tavassoli, A., Liu, J., & Sheikh, S. (2015). Glass Fiber-Reinforced Polymer-Reinforced Circular Columns under Simulated Seismic Loads. *ACI Structural Journal*, *112*(1).

Wu, W.-P. (1991). *Thermomechanical properties of fiber-reinforced plastic (FRP) bars*. West Virginia University.

Table 1 – Nominal and effective diameters of GFRP bars for various bar numbers and grades

Bar number/size	Grade	Nominal diameter, d_b (mm)	Effective diameter, d_e (mm)
#5 (15M)	I	15.9	15.6
	II		16.5
	III		17.2
#6 (20M)	I	19.0	18.5
	II		19.8
	III		20.4
#8 (25M)	I	25.5	24.7
	II		26
	III		27

Table 2 – Physical properties of GFRP bars

Property		**Grade I**			**Grade II**			**Grade III**		
#5 (15M)	unit	Average	SD	CoV (%)	Average	SD	CoV (%)	Average	SD	CoV (%)
Fiber mass content*	%	84	0.3	0.4	85	0.1	0.1	84	1.1	1.3
Glass transition temperature**	^{o}C	113	2.1	1.9	120	8.4	7.0	109	4.5	4.1
Measured cross-sectional area***	mm^2	188	1.1	0.6	203	0.4	0.2	234	5.4	2.3
Moisture absorption in 24hrs****	%	0.05	0.002	4.0	0.05	0.002	4.0	0.03	0.001	3.3
#6 (20M)	unit	Average	SD	CoV (%)	Average	SD	CoV (%)	Average	SD	CoV (%)
Fiber mass content	%	84	0.4	0.5	84	0.3	0.4	84	0.1	0.1
Glass transition temperature	^{o}C	111	2.8	2.5	110	3.1	2.8	121	5.4	4.5
Measured cross-sectional area	mm^2	280	4	1.4	293	3.4	1.2	345	0.3	0.1
Moisture absorption in 24hrs	%	0.04	0.001	2.5	0.06	0.002	3.3	0.04	0.002	5.0
#8 (25M)	unit	Average	SD	CoV (%)	Average	SD	CoV (%)	Average	SD	CoV (%)
Fiber mass content	%	85	0.1	0.1	86	0.0	0.0	86	0.1	0.1
Glass transition temperature	^{o}C	115	5.3	4.6	122	3.8	3.1	109	2.5	2.3
Measured cross-sectional area	mm^2	486	1.7	0.3	536	0.8	0.1	567	0.5	0.1
Moisture absorption in 24hrs	%	0.04	0.002	5.0	0.03	0.002	6.7	0.03	0.005	16.7

*ASTM D2584 (ASTM, 2018), **ASTM E1356 (ASTM, 2014), ***ASTM D7205 (ASTM, 2021), ****ASTM D570 (ASTM, 2022)

Table 3 – Results of tensile tests by the manufacturer according to ASTM D7205 (ASTM, 2021)

Property		**Grade I**			**Grade II**			**Grade III**		
#5 (15M)	unit	Average	SD	CoV (%)	Average	SD	CoV (%)	Average	SD	CoV (%)
Ultimate tensile strength	MPa	962	22.8	2.4	1119	25.9	2.3	1281	40.4	3.2
Tensile elastic modulus	MPa	48558	360	0.7	53739	90.1	0.2	63883	1405.4	2.2
Ultimate tensile strain	%	2	0.05	2.5	2.1	0.05	2.4	2	0.03	1.5
#6 (20M)	unit	Average	SD	CoV (%)	Average	SD	CoV (%)	Average	SD	CoV (%)
Ultimate tensile strength	MPa	1056	14.6	1.4	1084	46.5	4.3	1313	33.1	2.5
Tensile elastic modulus	MPa	50354	145.2	0.3	54563	708.6	1.3	63807	580.8	0.9
Ultimate tensile strain	%	2.1	0.02	1.0	2	0.1	5.0	2.1	0.04	1.9
#8 (25M)	unit	Average	SD	CoV (%)	Average	SD	CoV (%)	Average	SD	CoV (%)
Ultimate tensile strength	MPa	962	8.2	0.9	1030	16.5	1.6	1143	25.4	2.2
Tensile elastic modulus	MPa	50123	688.7	1.4	57725	756	1.3	60904	475.5	0.8
Ultimate tensile strain	%	1.9	0.04	2.1	1.8	0.04	2.2	1.9	0.05	2.6

Table 4 – Results of compression tests using the proposed fixture for L/d_b=2

Bar number/size	Grade	f_{fc} (MPa)	f_{fc}/f_{ft}	E_{fc} (GPa)	E_{fc}/E_{ft}	ε_{fcu} (-)	$\varepsilon_{fcu}/\varepsilon_{ftu}$
#5 (15M)	I	918	0.95	52.3	1.08	0.018	0.88
		970	1.01	46.4	0.96	0.020	0.99
		851	0.89	49.3	1.02	0.016	0.79
		896	0.93	47.8	0.98	0.018	0.91
		943	0.98	48.0	0.99	0.017	0.83
	Average	**915**	**0.95**	**49**	**1.00**	**0.018**	**0.88**
	SD	**45**	**0.05**	**2.2**	**0.05**	**0.002**	**0.08**
	CoV (%)	**4.9**	**4.9**	**4.6**	**4.6**	**8.9**	**8.9**
	II	956	0.85	50.3	0.94	0.019	0.91
		946	0.85	49.2	0.92	0.020	0.95
		847	0.76	51.0	0.95	0.016	0.77
		996	0.89	50.5	0.94	0.020	0.95
		1017	0.91	49.6	0.92	0.016	0.74
	Average	**952**	**0.85**	**50**	**0.93**	**0.018**	**0.86**
	SD	**66**	**0.06**	**0.7**	**0.01**	**0.002**	**0.10**
	CoV (%)	**6.9**	**6.9**	**1.4**	**1.4**	**11.6**	**11.6**
	III	999	0.78	63.3	0.99	0.016	0.80
		922	0.72	66.8	1.05	0.014	0.68
		929	0.73	64.0	1.00	0.015	0.75
		1314	1.03	66.8	1.05	0.018	0.92
		1187	0.93	67.0	1.05	0.014	0.72
	Average	**1070**	**0.84**	**66**	**1.03**	**0.015**	**0.77**
	SD	**173**	**0.14**	**1.8**	**0.03**	**0.002**	**0.09**
	CoV (%)	**16.2**	**16.2**	**2.7**	**2.7**	**11.7**	**11.7**
#6 (20M)	I	893	0.85	49.0	0.97	0.018	0.85
		917	0.87	49.3	0.98	0.018	0.84
		946	0.90	50.3	1.00	0.019	0.93
		968	0.92	49.5	0.98	0.021	0.99
		966	0.91	48.4	0.96	0.020	0.93
	Average	**938**	**0.89**	**49**	**0.98**	**0.019**	**0.91**
	SD	**32**	**0.03**	**0.7**	**0.01**	**0.001**	**0.06**
	CoV	**3.4**	**3.4**	**1.4**	**1.4**	**7.0**	**7.0**
	II	981	0.90	53.9	0.99	0.014	0.72
		901	0.83	51.9	0.95	0.016	0.80
		900	0.83	50.9	0.93	0.017	0.86
		934	0.86	54.8	1.00	0.017	0.85
		902	0.83	53.9	0.99	0.016	0.80
	Average	**924**	**0.85**	**53**	**0.97**	**0.016**	**0.81**
	SD	**35**	**0.03**	**1.6**	**0.03**	**0.001**	**0.06**
	CoV	**3.8**	**3.8**	**3.0**	**3.0**	**7.4**	**7.4**
	III	1127	0.86	60.6	0.95	0.019	0.90
		1227	0.93	59.7	0.94	0.017	0.83
		1148	0.87	58.1	0.91	0.019	0.90
		1186	0.90	60.2	0.94	0.019	0.90
		1163	0.89	58.1	0.91	0.019	0.89
	Average	**1170**	**0.89**	**59**	**0.93**	**0.019**	**0.88**
	SD	**39**	**0.03**	**1.2**	**0.02**	**0.001**	**0.03**
	CoV (%)	**3.3**	**3.3**	**2.0**	**2.0**	**3.5**	**3.5**
#8 (25M)	I	677	0.70	47.0	0.94	0.014	0.76
		786	0.82	51.0	1.02	0.017	0.88
		763	0.79	46.6	0.93	0.016	0.82
		782	0.81	46.5	0.93	0.016	0.86
		786	0.82	47.9	0.96	0.016	0.86
	Average	**759**	**0.79**	**48**	**0.95**	**0.016**	**0.84**
	SD	**46**	**0.05**	**1.9**	**0.04**	**0.001**	**0.05**

	CoV (%)	**6.1**	**6.1**	**3.9**	**3.9**	**5.8**	**5.8**
	II	953	0.92	59.3	1.03	0.014	0.80
		873	0.85	53.5	0.93	0.016	0.86
		897	0.87	59.0	1.02	0.016	0.87
		947	0.92	56.7	0.98	0.016	0.90
		800	0.78	57.4	0.99	0.015	0.84
	Average	**894**	**0.87**	**57**	**0.99**	**0.015**	**0.85**
	SD	**63**	**0.06**	**2.3**	**0.04**	**0.001**	**0.04**
	CoV (%)	**7.0**	**7.0**	**4.1**	**4.1**	**4.6**	**4.6**
	III	994	0.87	58.6	0.96	0.016	0.86
		922	0.81	58.4	0.96	0.016	0.83
		938	0.82	57.2	0.94	0.013	0.68
		911	0.80	61.6	1.01	0.016	0.83
		945	0.83	62.0	1.02	0.015	0.80
	Average	**942**	**0.82**	**60**	**0.98**	**0.015**	**0.80**
	SD	**32**	**0.03**	**2.1**	**0.03**	**0.001**	**0.07**
	CoV (%)	**3.4**	**3.4**	**3.6**	**3.6**	**8.9**	**8.9**
Overall	Average	**-**	**0.86**	**-**	**0.97**	**-**	**0.85**
	SD	**-**	**0.047**	**-**	**0.032**	**-**	**0.045**
	CoV (%)	**-**	**5.4**	**-**	**3.3**	**-**	**5.3**

Average, Standard Deviation (SD), and Coefficient of Variation (CoV) values are boldfaced for clarity and easier distinction.

Table 5 – Results of compression tests for L/d_b of 4 and 6

Test Number	L/d_b	f_{fc} (MPa)	f_{fc}/f_{ft}	E_c (GPa)	E_c/E_t
1	4	803	0.72	52.9	0.98
2		838	0.75	54.2	1.01
3		890	0.80	53.8	1.00
4		853	0.76	52.5	0.98
5		981	0.88	43.9	0.82
6		811	0.72	49.1	0.91
7		874	0.78	50.2	0.93
8		936	0.84	49.2	0.92
Average		**873**	**0.78**	**50.7**	**0.94**
SD		**61**	**0.05**	**3.4**	**0.06**
CoV (%)		**7**	**7**	**7**	**7**
1	6	817	0.73	55.3	1.03
2		662	0.59	49.7	0.92
3		778	0.70	55.1	1.03
4		635	0.57	48.6	0.90
5		576	0.51	47.9	0.89
6		583	0.52	44.9	0.84
7		725	0.65	44.9	0.84
8		849	0.76	49.4	0.92
Average		**703**	**0.63**	**49.5**	**0.92**
SD		**105**	**0.09**	**4.0**	**0.07**
CoV (%)		**15**	**15**	**8**	**8**

Table 6 – ANOVA table for the ratio of f_{fc}/f_{ft} in this study versus other studies

Source of Variation	Count	Average	Variance	SS	df	MS	F	P-value	F crit
Between Groups	11	0.8328	0.0069	0.2522	1	0.2522	10.6751	0.0021	4.0518
Within Groups	37	0.6603	0.0283	1.0866	46	0.0236			
Total				1.3388	47				

SS: Sum of Squares, which is the sum of the squared deviations from the mean, used to calculate the variance.
df: Degrees of Freedom, which indicates the number of independent pieces of information available for estimating statistical parameters.
MS: Mean Square, which is the variance divided by its degrees of freedom, providing an estimate of the population variance.

Table 7 – ANOVA table for the ratio of E_{fc}/E_{ft} in this study versus other studies

Source of Variation	Count	Average	Variance	SS	df	MS	F	P-value	F crit
Between Groups	11	0.9661	0.0011	0.0228	1	0.0228	4.8587	0.0326	4.0518
Within Groups	37	1.0180	0.0057	0.2158	46	0.0047			
Total				0.2386	47				

SS: Sum of Squares, which is the sum of the squared deviations from the mean, used to calculate the variance.
df: Degrees of Freedom, which indicates the number of independent pieces of information available for estimating statistical parameters.
MS: Mean Square, which is the variance divided by its degrees of freedom, providing an estimate of the population variance.

List of figures:

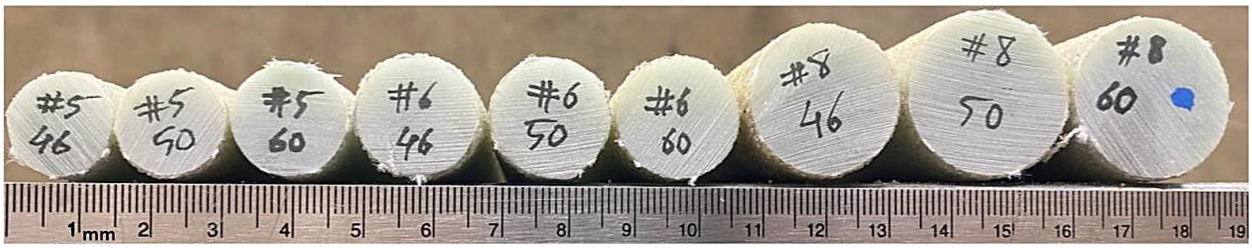

Figure 1 – Cross-sectional view of the bar specimens

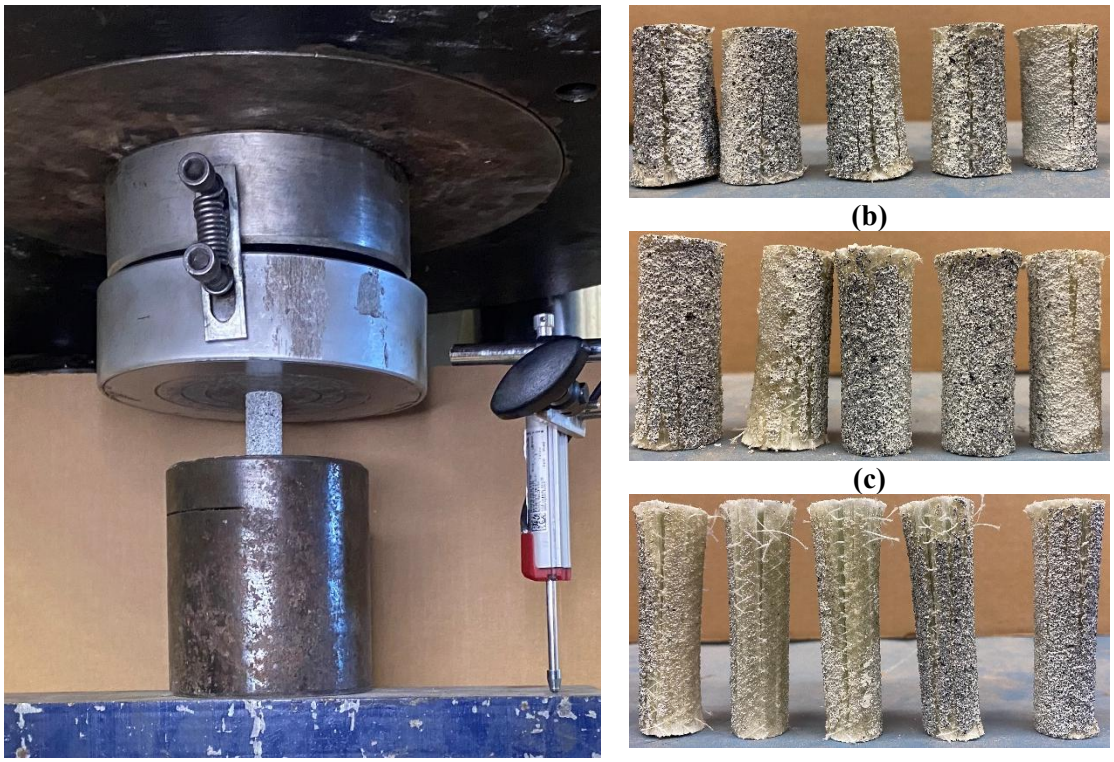

(a) **(b)** **(c)** **(d)**

Figure 2 – The first series of initial tests: a) Test setup, b) Failed specimens of L/d_b=2, c) Failed specimens of L/d_b=2.75, and d) Failed specimens of L/d_b=4 (The longitudinal splitting as the governing failure mode is obvious.)

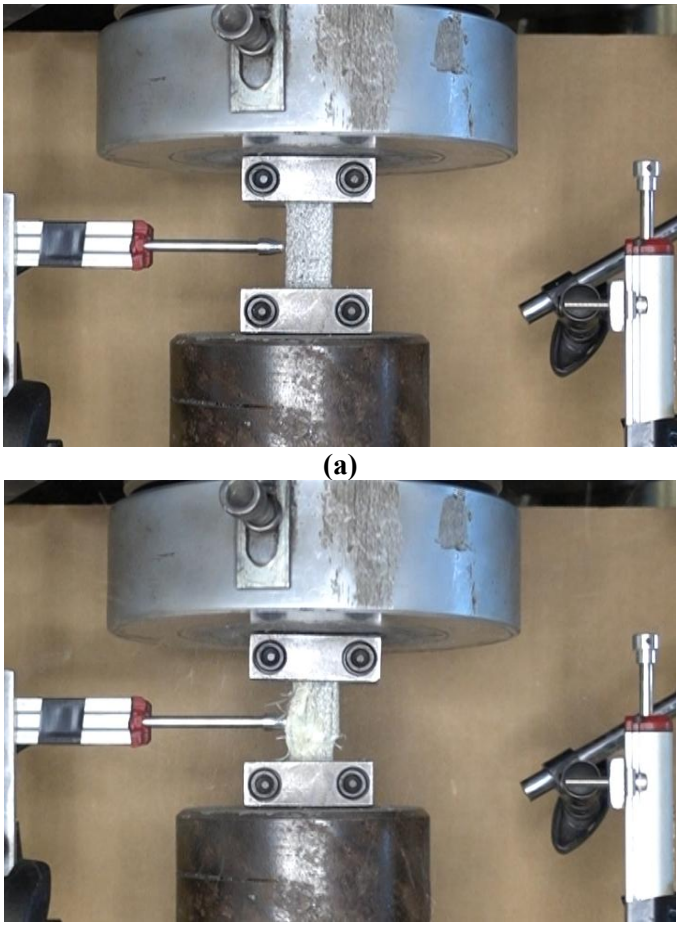

Figure 3 – The test setup for the first fixture used to prevent the propagation of specimen's premature end failures: a) Before failure, b) At the failure moment (The scattering and dispersion of fiber particles are visible.)

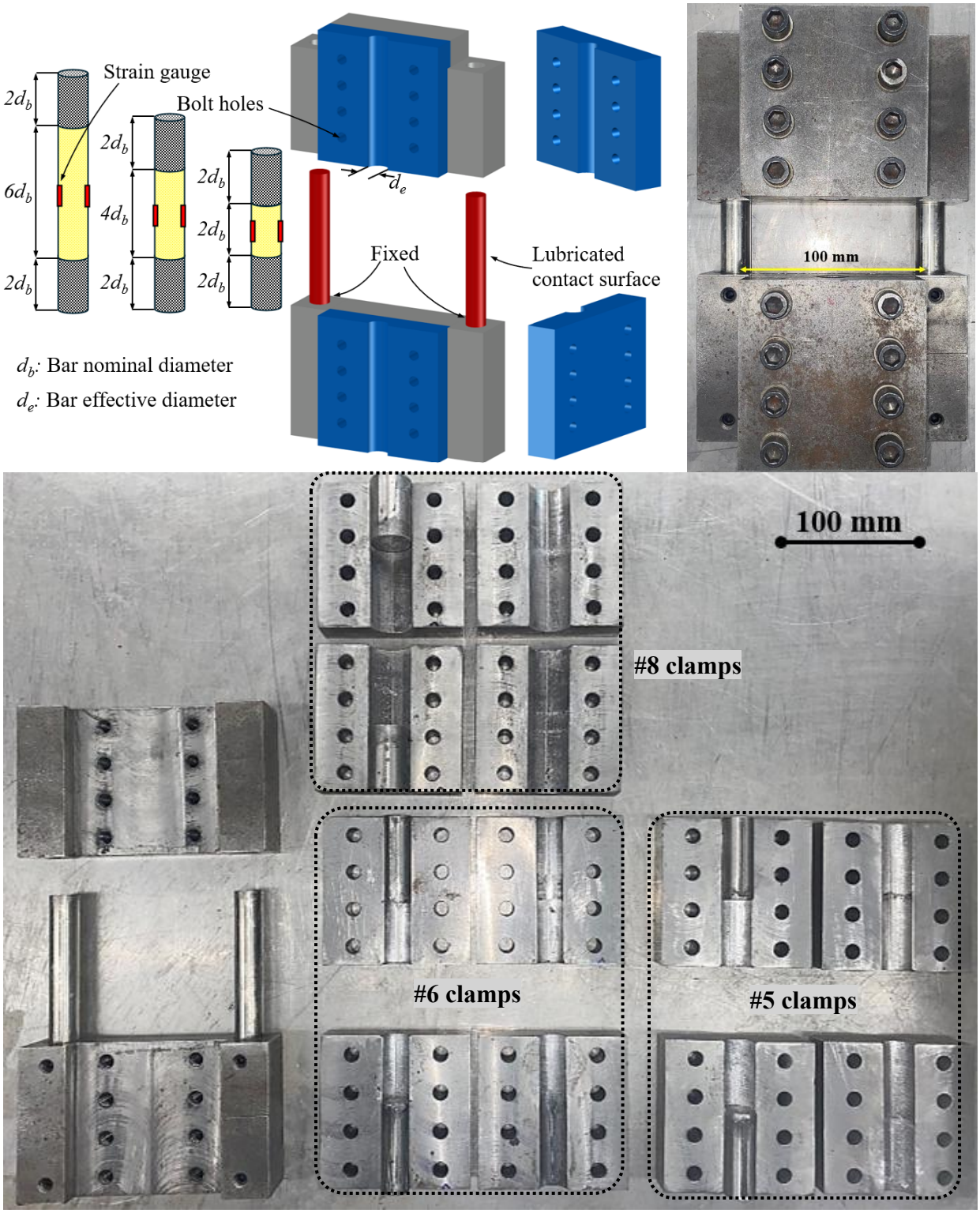

Figure 4 – Proposed test fixture

Cutting the bars

Filing

Tape wrapping

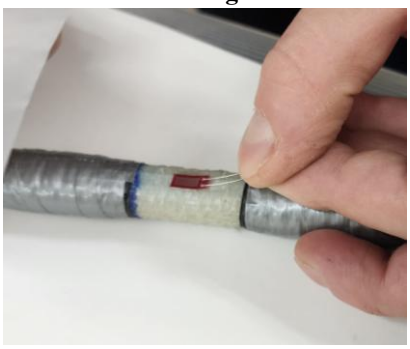

Strain gauge installation

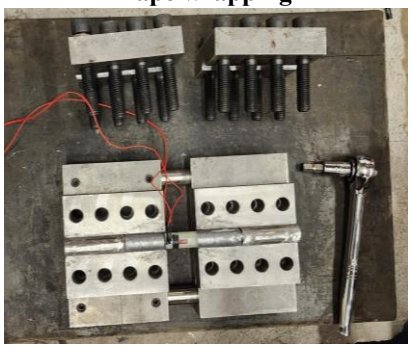

Positioning the bar

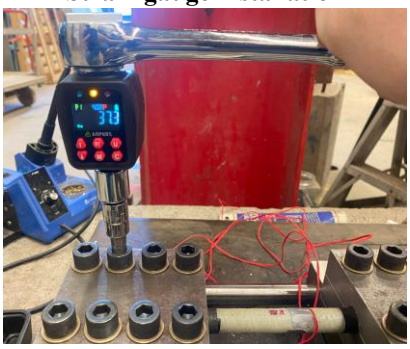

Tightening

Compression

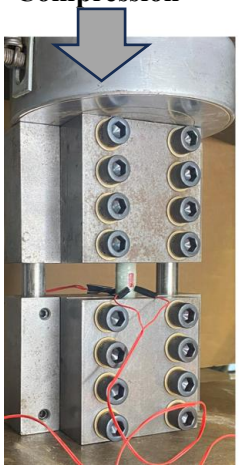

L/d_b=2

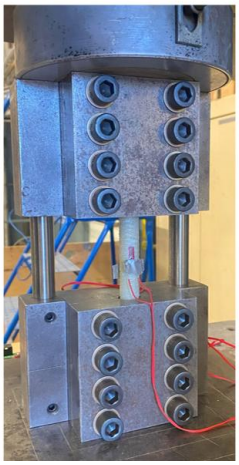

L/d_b=4

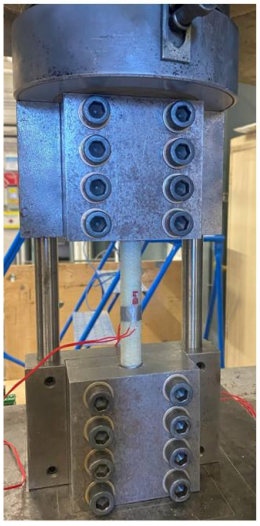

L/d_b=6

Figure 5 – Specimens preparation, clamping, and testing process for the compressive tests

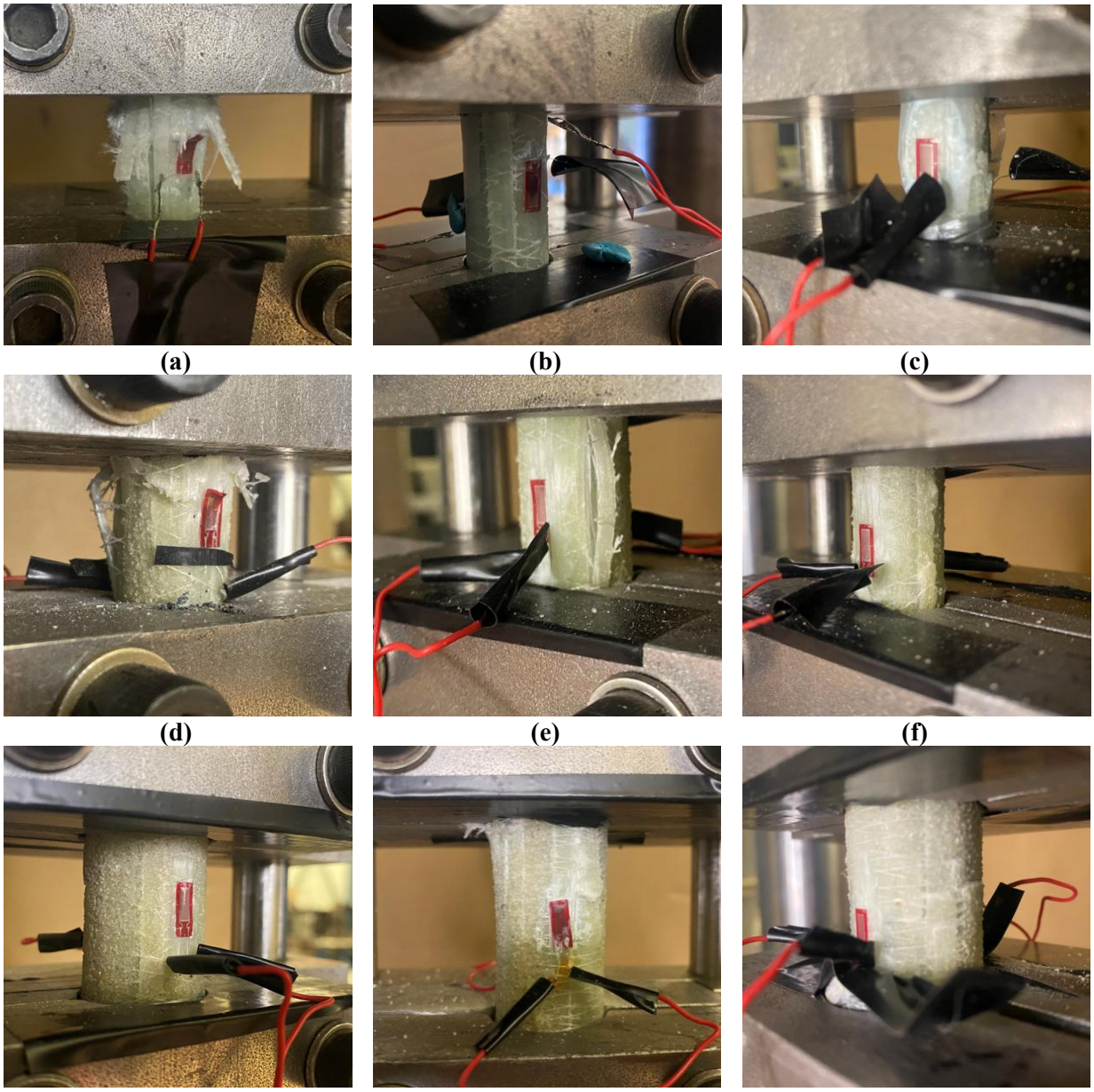

Figure 6 – Specimens' failure modes after tests: a) #5-Grade I, b) #5-Grade II, c) #5-Grade III, d) #6-Grade I, e) #6-Grade II, f) #6-Grade III, g) #8-Grade I, h) #8-Grade II, i) #8-Grade III

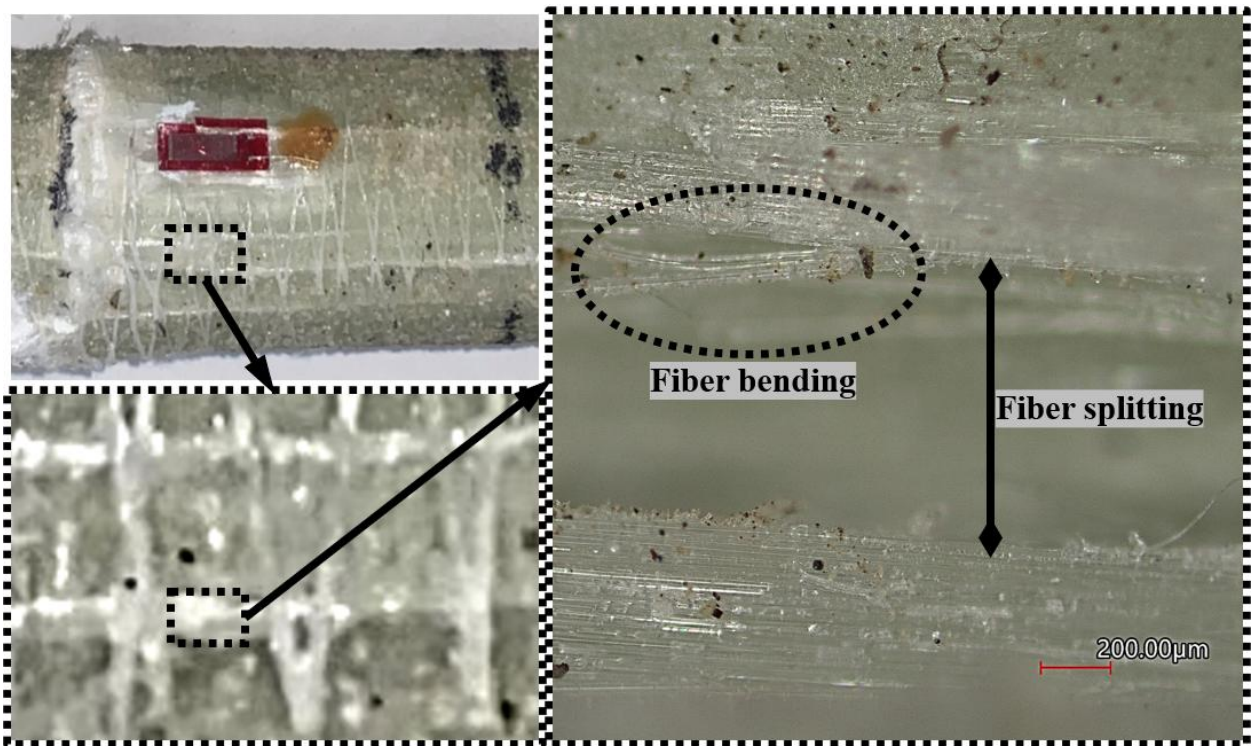

Figure 7 – Longitudinal splitting and fiber bending

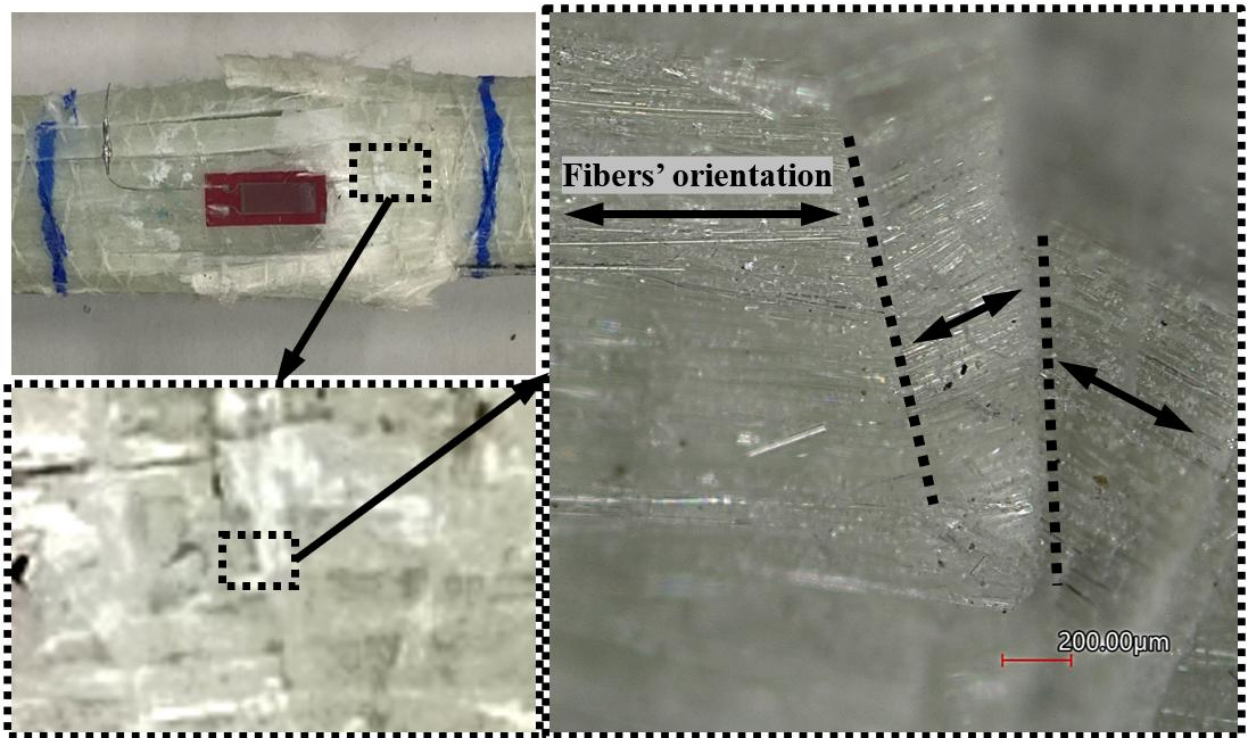

Figure 8 – Shear crippling and fiber kinking

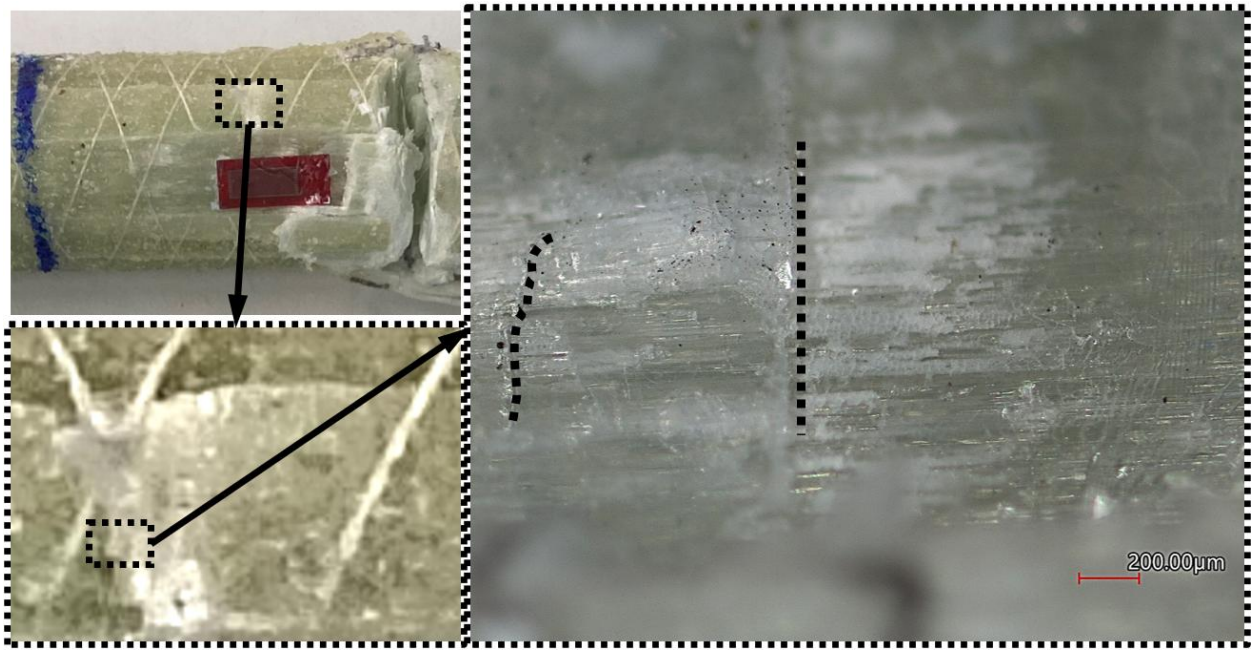

Figure 9 – Fiber compressive failure and matrix cracking

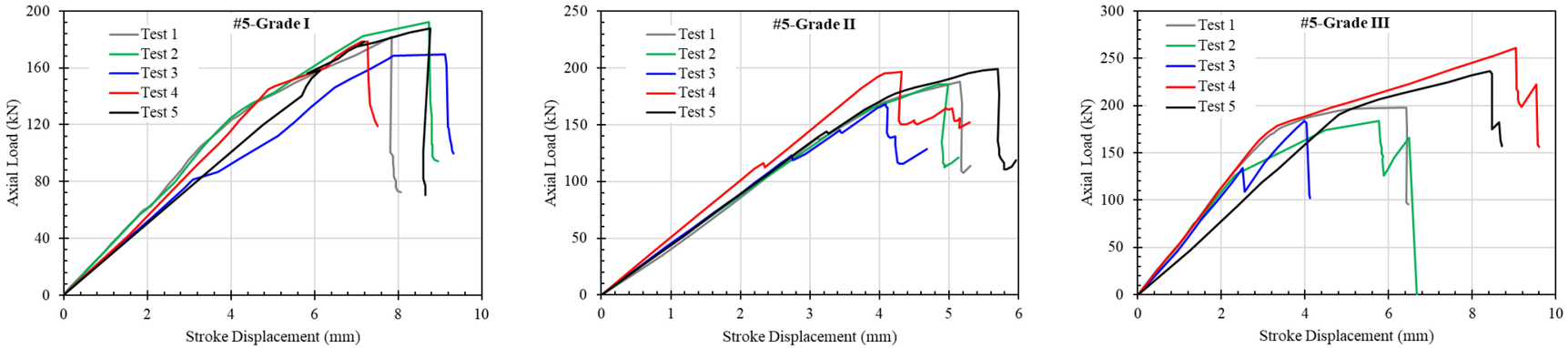

(a)

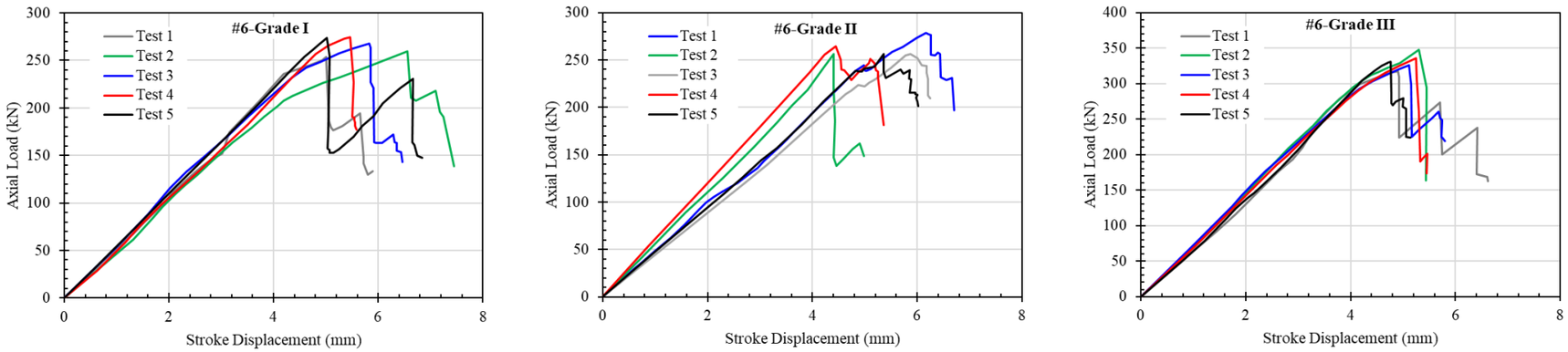

(b)

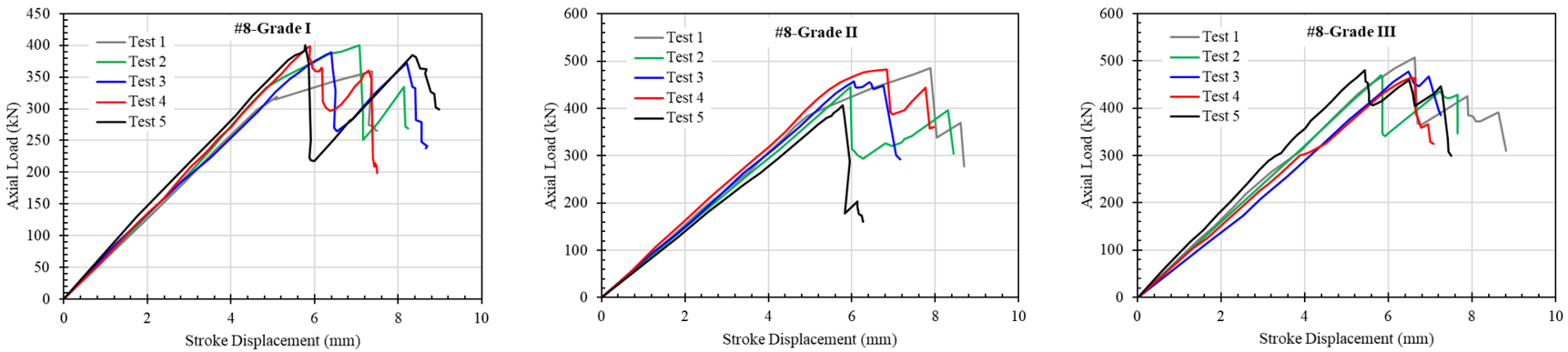

(c)

Figure 10 – Axial load vs. stroke displacement curves of compression tests: a) #5 (15M), b) #6 (20M), and c) #8 (25M)

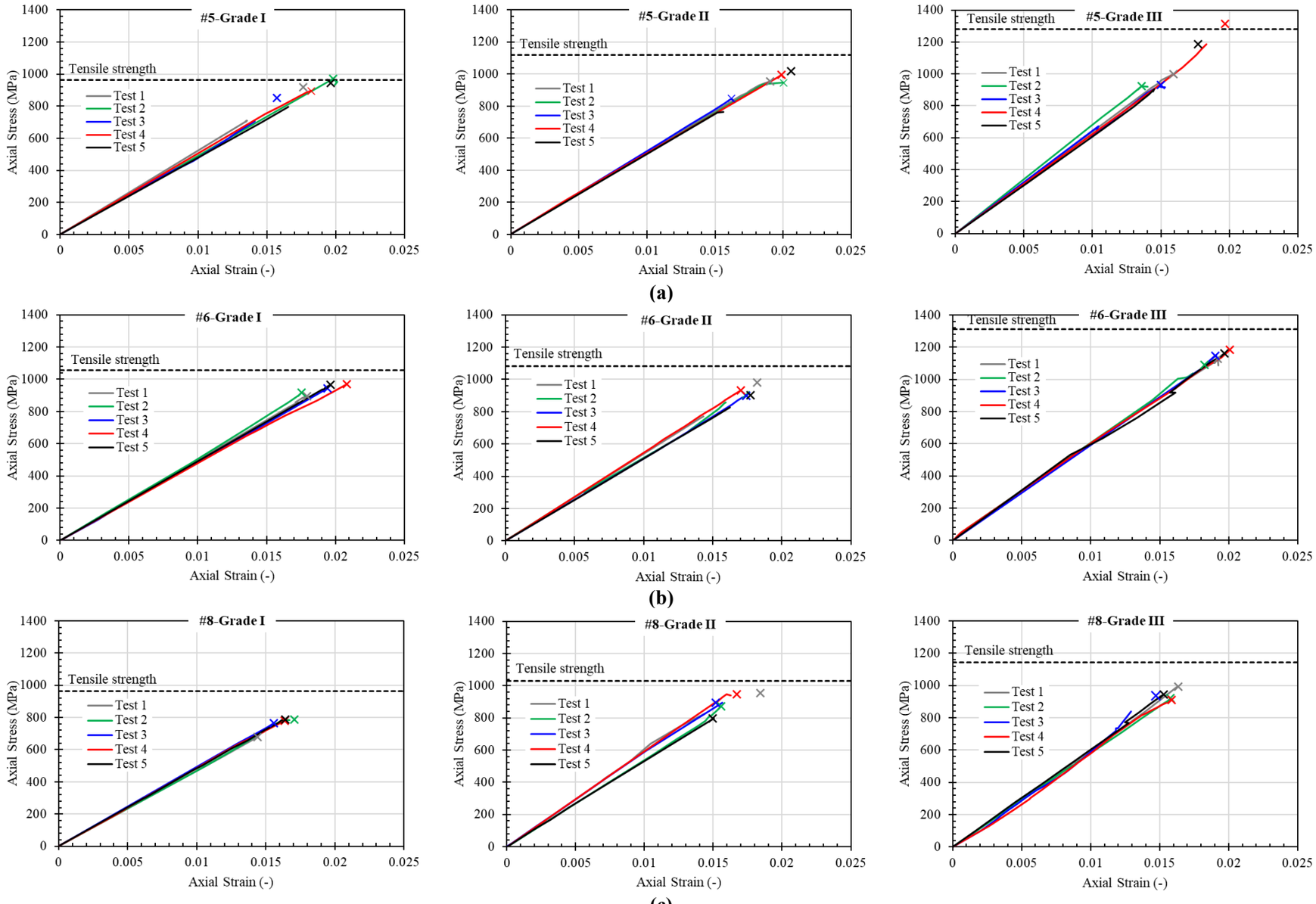

Figure 11 – Axial stress vs. average axial strain curves of compression tests: a) #5 (15M), b) #6 (20M), and c) #8 (25M)

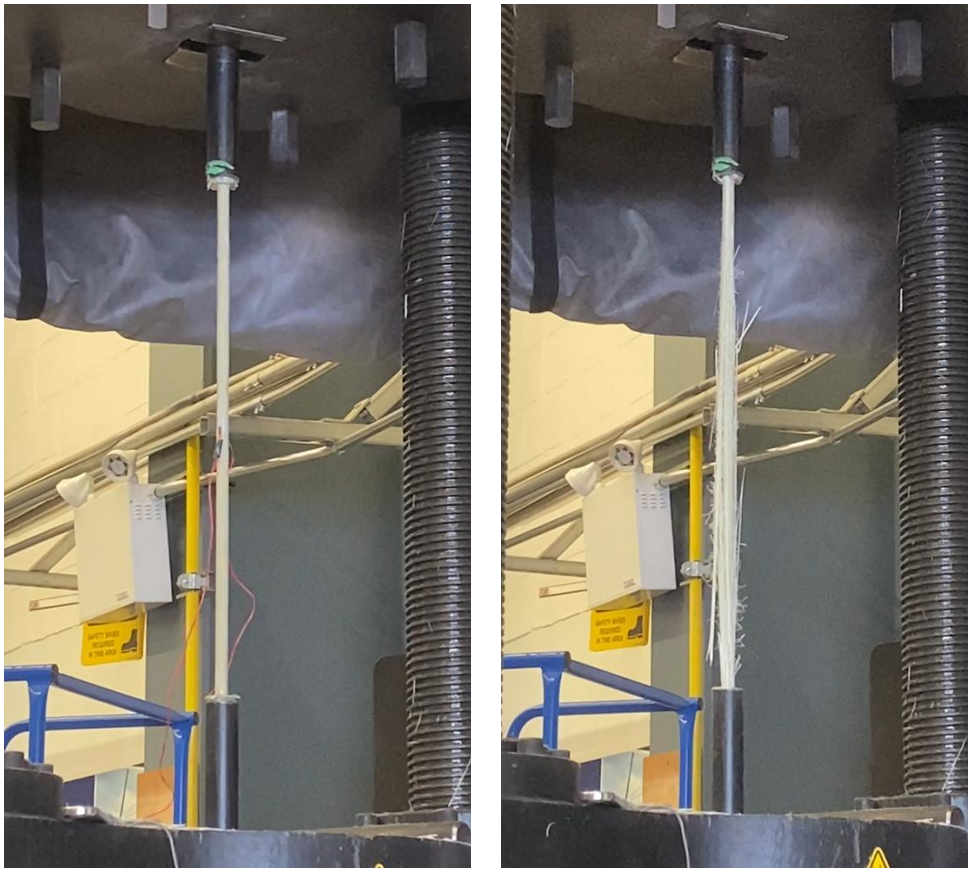

(a) **(b)**

Figure 12 – Tensile specimen test: a) Setup and instrumentation, b) Failure

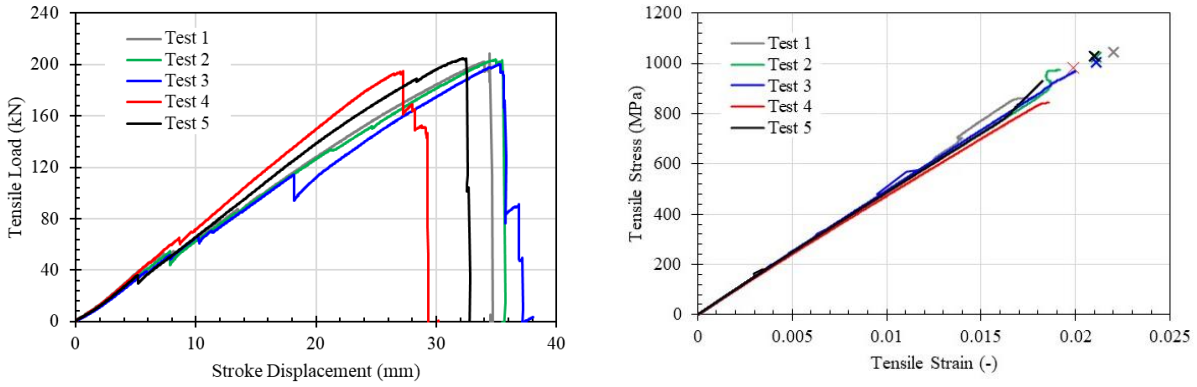

(a) **(b)**

Figure 13 – Results of tensile tests on #5 (15M) rebars (Grade II): a) Axial load vs. stroke displacement, b) Axial stress vs. average axial strain

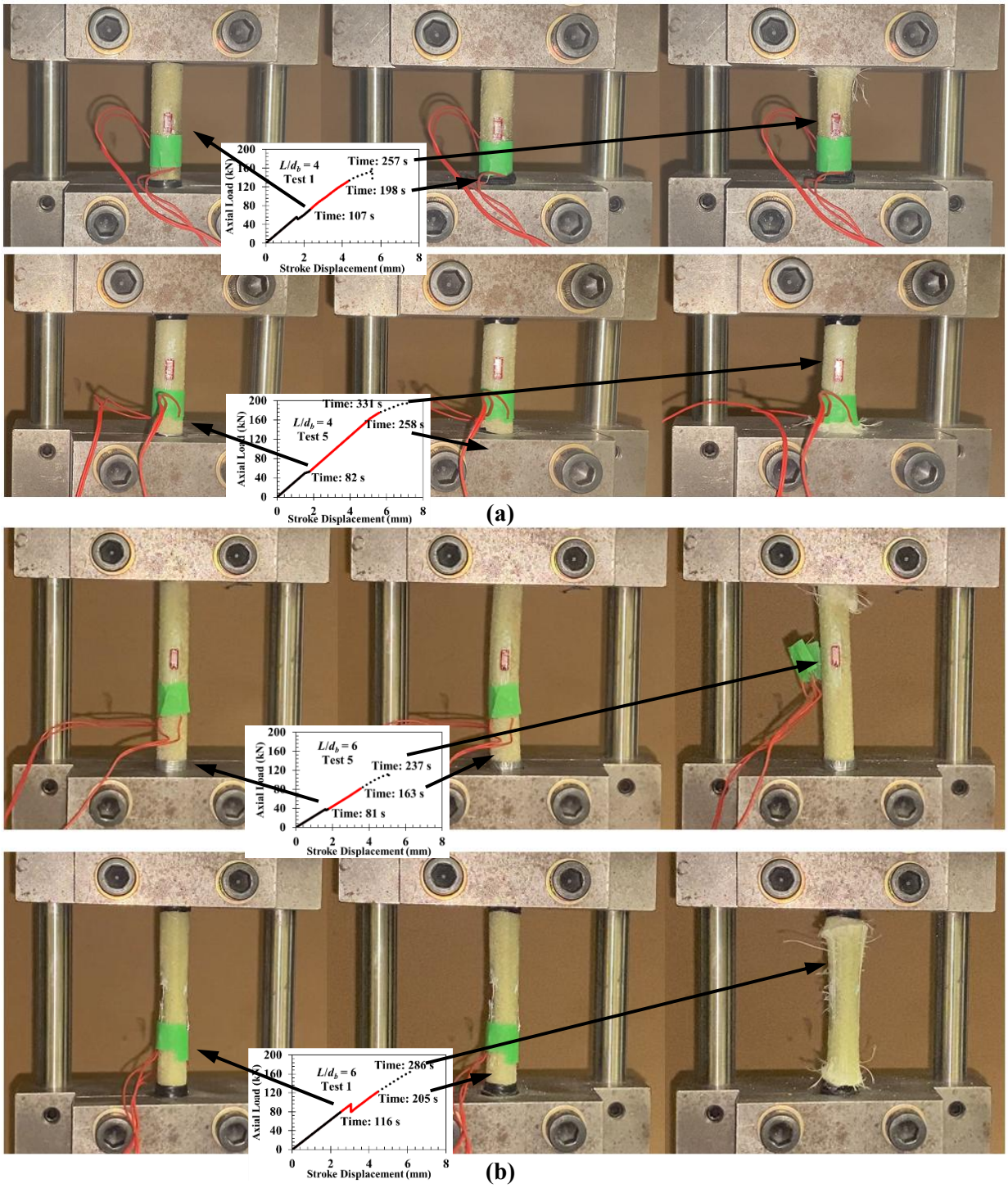

Figure 14 – Monitoring of specimen deformation in the gauge length for Test 1 and Test 5: a) L/d_b=4 and b) L/d_b=6

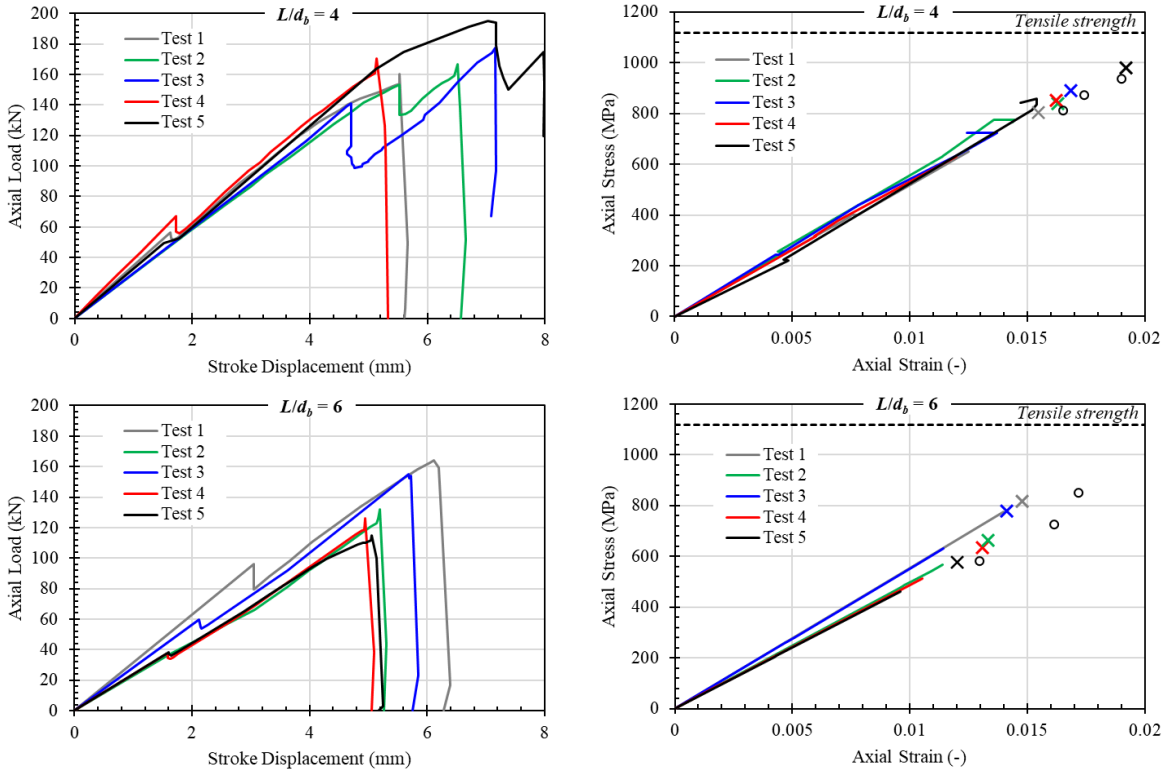

Figure 15 – Axial stress vs. average axial strain curves for L/d_b of 4 and 6

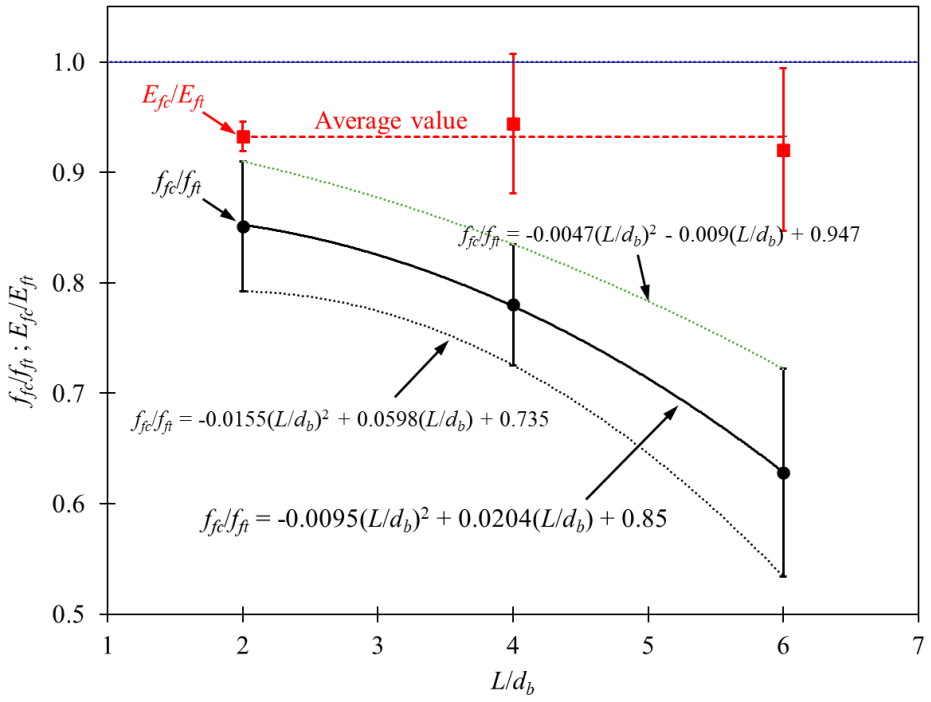

Figure 16 – Ratio of compressive to tensile strength and compressive to tensile modulus of elasticity for different length to diameter ratios

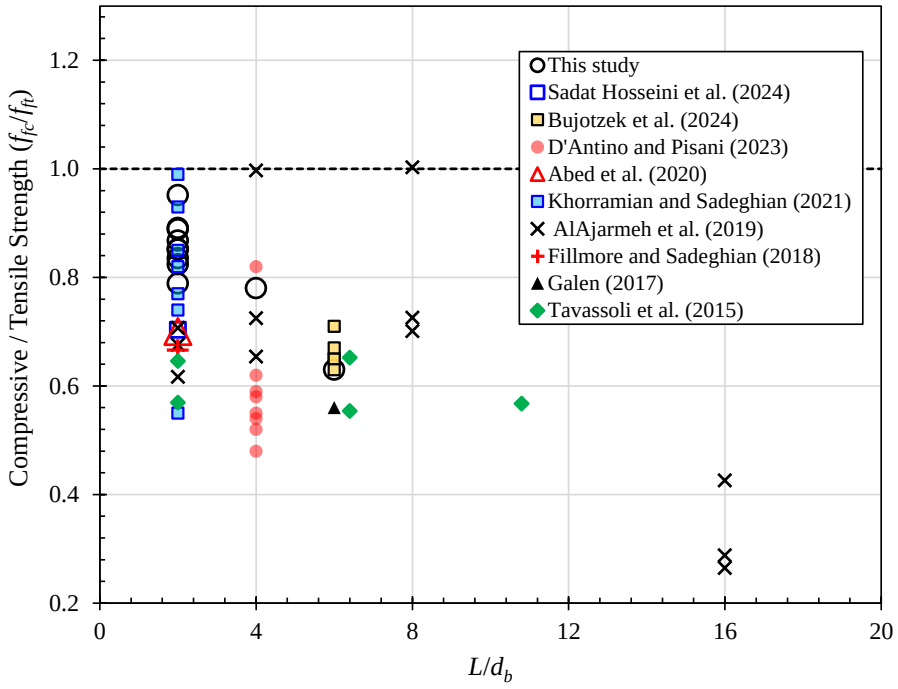

(a)

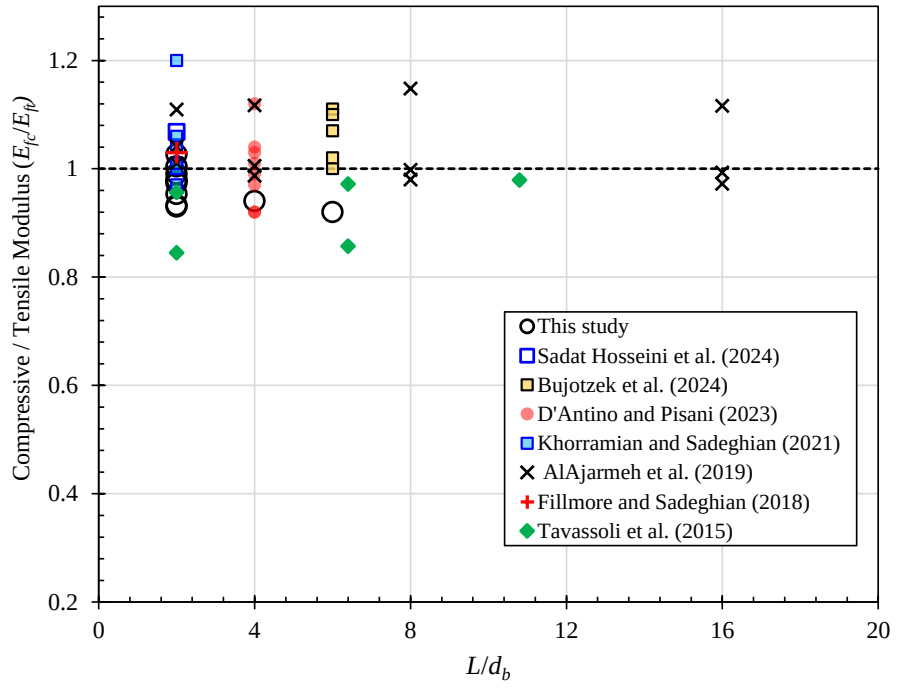

(b)

Figure 17 – Comparing the scattering of the data from this study and recent previous studies in the literature for f_{fc}/f_{ft} and E_{fc}/E_{ft}

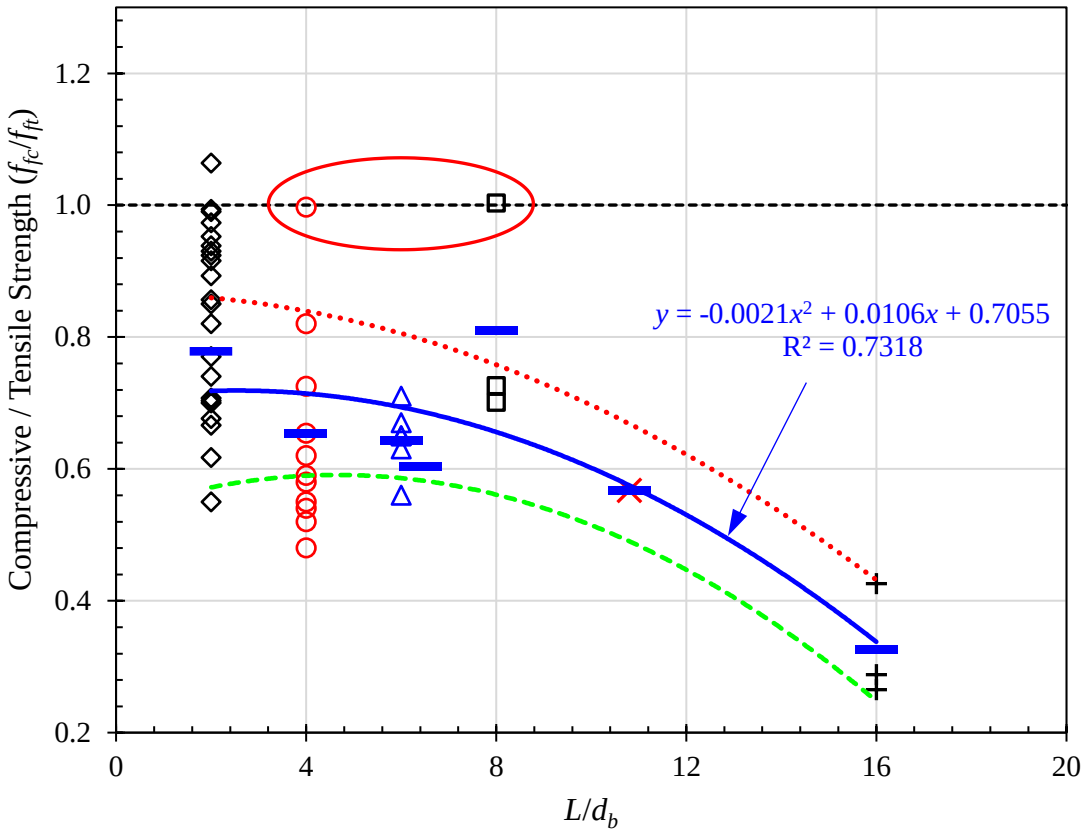

Figure 18 – Analysis of the overall data on compressive to tensile strength ratios across various L/d_b ratios

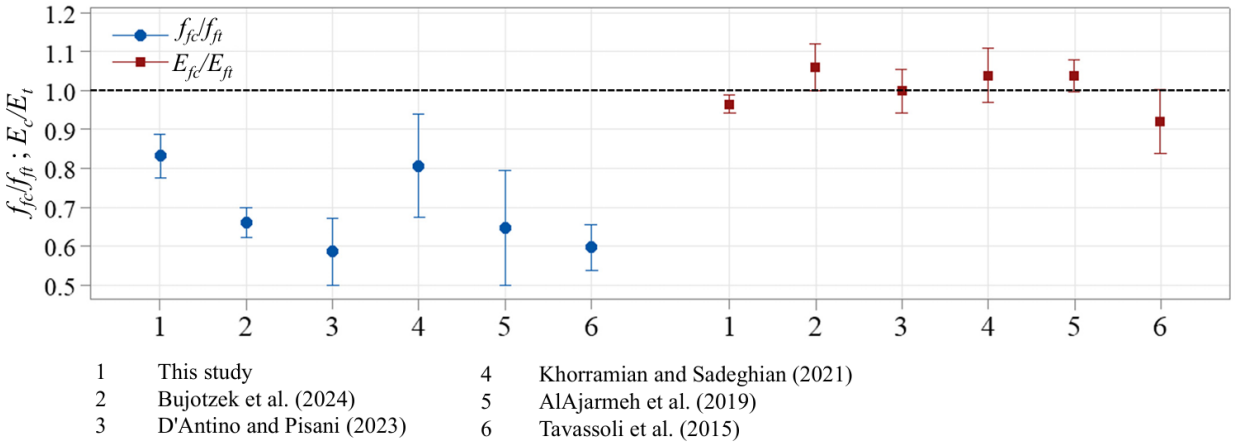

Figure 19 – Interval plots for f_{fc}/f_{ft} and E_{fc}/E_{ft}

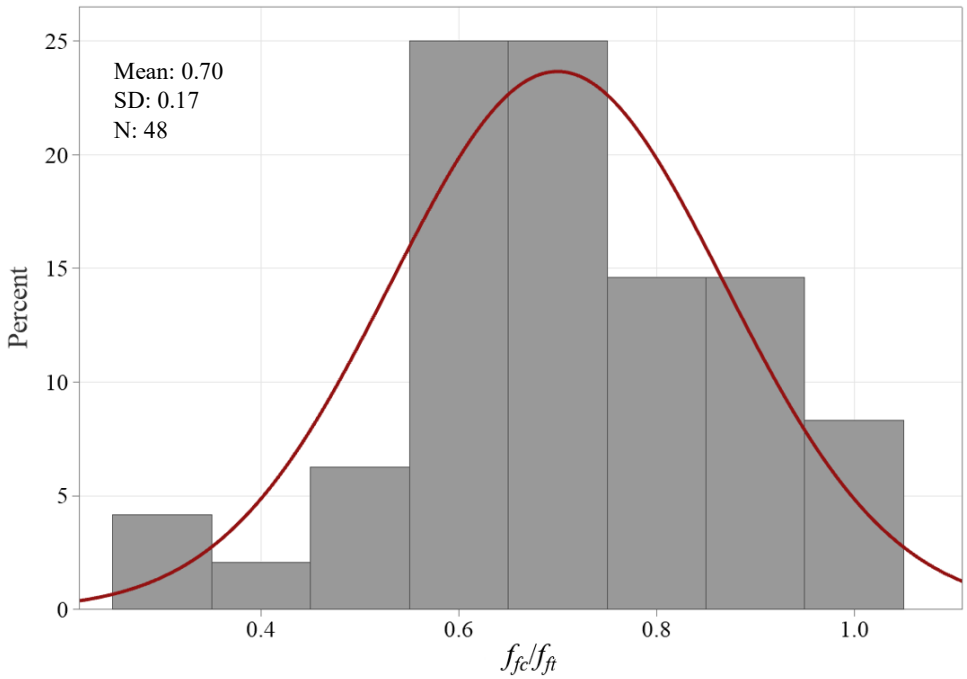

(a)

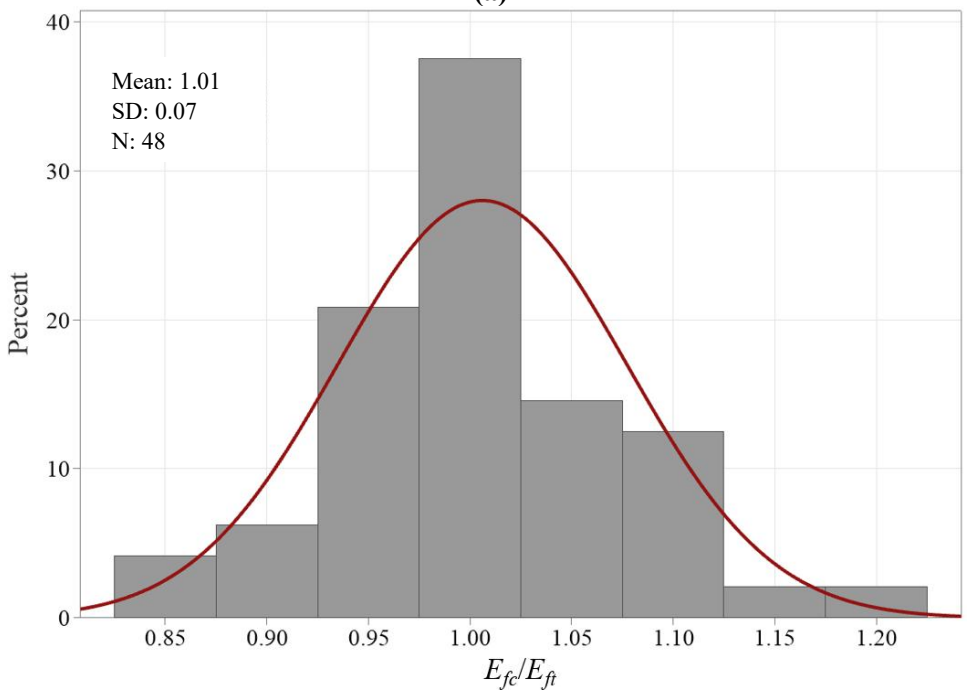

(b)

Figure 20 – Histograms of all data for a) f_{fc}/f_{ft} and b) E_{fc}/E_{ft}